separately identified, and the appropriate hydrogen-deuterium isotope shift was observed in the optical-mode characteristic temperature. The Hall effect and thermoelectric power data reveal majority hole conduction for the fcc hydride phase and majority electron conduction for the fct phase.

ACKNOWLEDGMENTS

We are indebted to G. W. Lehman and W. J. Tomasch for valuable discussions, to D. L. Henry for supplying specimens, and to D. H. Leslie for assistance with some of the measurements.

* Research supported in part by the U.S. Atomic Energy Commission.

† Deceased.

‡ Present address: Department of Physics, Colorado State University, Fort Collins, Colo. 80521.

[1] For references on the phase diagram of the Zr-H system see K. E. Moore and W. A. Young, J. Nucl. Mater. **27,** 316 (1968).

[2] H. E. Flotow and D. W. Osborne, J. Chem. Phys. **34,** 1418 (1961).

[3] W. J. Tomasch, Phys. Rev. **123,** 510 (1961).

[4] R. E. Rundle, C. G. Shull, and E. O. Woolan, Acta Cryst. **5,** 22 (1952).

[5] I. Pelah, C. M. Eisenhauer, D. J. Hughes, and H. Palevsky, Phys. Rev. **108,** 1091 (1957).

[6] A. Andresen, A. W. McReynolds, M. Nelkin, M. Rosenbluth, and W. Whittemore, Phys. Rev. **108,** 1092 (1957).

[7] W. L. Whittemore and A. W. McReynolds, Phys. Rev. **113,** 806 (1959).

[8] S. S. Sidhu, L. Heaton, and M. H. Mueller, J. Appl. Phys. **30,** 1323 (1959).

[9] For additional references on neutron scattering in zirconium hydride see S. S. Pan and F. J. Webb, J. Nucl. Sci. Eng. **23,** 194 (1965).

[10] P. W. Bickel and T. G. Berlincourt, Phys. Rev. **119,** 1603 (1960).

[11] P. W. Bickel, U.S. Atomic Energy Commission Report No. NAA-SR-4173, 1960 (unpublished).

[12] V. I. Savin, R. A. Andriyevskiy, Y. B. Boyko, and R. A. Lyutikov, Phys. Metals Metallog. (USSR) **24,** 54 (1967).

[13] R. A. Andrievskii, E. B. Boiko, and R. B. Ioffe, Izv. Akad. Nauk SSSR, Neorg. Mater. **3,** 1591 (1967).

[14] G. L. Miller, *Zirconium*, 2nd ed. (Academic, New York, 1957), pp. 267–272.

[15] J. B. Vetrano, U.S. Atomic Energy Commission Report No. BMI-1243, 1957 (unpublished).

[16] O. Lindberg, Proc. Inst. Radio Engrs. **40,** 1414 (1952).

[17] T. G. Berlincourt, Phys. Rev. **112,** 381 (1958).

[18] T. G. Berlincourt, Phys. Rev. **114,** 969 (1959).

[19] J. W. Christians, J. P. Jan, W. B. Pearson, and I. M. Templeton, Proc. Roy. Soc. (London) **A245,** 213 (1958).

[20] C. D. Hodgman, *Handbook of Chemistry and Physics*, 39th ed. (Chemical Rubber Publishing Co., Cleveland, 1957), p. 2234.

[21] K. P. Singh and J. Gordon Parr, Trans. Faraday Soc. **59,** 2256 (1963).

[22] N. F. Mott and H. Jones, *The Theory of the Properties of Metals and Alloys* (Dover, New York, 1936), pp. 296–300.

[23] G. J. Dienes and G. H. Vineyard, *Radiation Effects in Solids* (Interscience, New York, 1957), p. 66.

[24] N. F. Mott and H. Jones, *The Theory of the Properties of Metals and Alloys* (Dover, New York, 1936), Chap. 7, p. 240.

[25] D. J. Howarth and E. H. Sondheimer, Proc. Roy. Soc. (London) **A219,** 53 (1953).

[26] For a discussion of various models for the phonon dispersion in ZrH_2, see E. L. Slaggie, J. Phys. Chem. Solids **29,** 923 (1968).

[27] U. Schmidt, Atomkernenergie **12,** 385 (1967).

[28] B. R. Coles, Phys. Rev. **101,** 1254 (1956).

[29] A. H. Wilson, *The Theory of Metals*, 2nd ed. (Cambridge U. P., London, 1954), pp. 193–249.

PHYSICAL REVIEW B VOLUME 2, NUMBER 12 15 DECEMBER 1970

de Haas–van Alphen Effect in Platinum*

J. B. KETTERSON AND L. R. WINDMILLER

Argonne National Laboratory, Argonne, Illinois 60439

(Received 22 April 1970)

The de Haas–van Alphen effect has been used to study the extremal areas, cyclotron masses, and spin-splitting zeros on all three sheets of the Fermi surface of platinum. For the Γ-centered electron surface and *X*-centered hole pocket, newly developed inversion techniques have been employed to obtain the Fermi radius and Fermi velocity at all points on these surfaces. By performing the appropriate integrations over these surfaces, we have been able to determine the number of carriers and the density of states for these surfaces. Our observations on the open-hole surface, when combined with band-structure calculations, confirm the shape and connectivity of this surface. By combining effective-mass data with spin-splitting zero data, we have obtained information on the magnitude and anisotropy of the *g* factor on all surfaces. In general, we find the *g* factor to be different from 2.0 and quite anisotropic. The effective-mass measurements, when compared with band-structure calculations, indicate an enhancement of approximately 30%.

I. INTRODUCTION

The de Haas–van Alphen effect has proved to be a powerful tool for the determination of the Fermi surfaces of metals. Traditional measurements yield the cross-sectional areas of the Fermi surface in planes normal to the magnetic field. Recently however, this effect has been shown to be capable of yielding detailed measurements of the cyclotron mass, Dingle-Robinson temperature, and *g* factor of electrons on the Fermi surface. With such information available, studies of the de Haas–van Alphen (dHvA) effect in metals now appear useful not only for determining the shape of the Fermi surface, but also for determining the limitations of the one-electron model calculations and estimating the magnitude of the many-body interactions. Pt is a metal especially suitable for such a program since it is known from the heat capacity[1,2] and the magnetic sus-

ceptibility[2,3] that the density of states at the Fermi level is anomalously high, suggesting that the one-electron bands may be considerably modified by the many-body interactions.

The electronic configuration of the ground state of Pt is $5d^9 6s^1$. Since the ground state of the atom contains both an unfilled d and s shell at nearly the same energy, we may reasonably expect the solid to contain both unfilled d-like and s-like bands. Such a situation makes the band-structure calculations more difficult for the following reason. In the atom the d-electron wavefunction is more localized than is the s-electron wave function. Thus, while a representation of the s-electron wave function in the solid in terms of a few plane waves (or orthogonalized plane waves) might work reasonably well, such a representation for the d-electron wave function would certainly be inadequate. The atomic d wave function is not, however, so localized that we would expect a tight-binding approach to be completely satisfactory either. Thus, a quantitative treatment of the energy bands in platinum (or any transition metal for that matter) requires a more powerful technique than the nearly-free-electron or tight-binding methods. Powerful first-principles calculational techniques are available in the augmented plane wave method (APW), its relativistic generalization (RAPW), and the KKR technique. Andersen and Mackintosh[4] have made extensive RAPW calculations in Pt that are in remarkably good quantitative agreement with the experimental data to be presented here. These calculations will be discussed later in this paper. The KKR technique, although quite powerful, has not until recently had much application.

There is a second approach to the determination of energy bands in solids. In this approach the philosophy is to find some appropriate parametrization of the energy bands. Then the band structure is generated by a two-step procedure. First, an initial set of parameters is obtained by fitting to the best available first-principles calculation. The parameters are then varied in order to produce a best fit to the experimentally determined Fermi surface. The "interpolation scheme"[5] is an example of this approach and has recently been applied to Pt with considerable success. The APW and KKR techniques are amenable to parametrization and will doubtless be applied to Pt in the future.

All the techniques described above calculate the energy bands in the one-electron approximation. Thus, electron correlation and the effects of a nonrigid lattice (electron-phonon interaction) are not included explicitly. Theory shows that the shape of the Fermi surface (Fermi momentum) is essentially unaffected by these many-body interactions provided the properly self-consistent one-electron potential is used to calculate the energy bands.[6] The Fermi velocity, however, is quite strongly modified by electronic (quasiparticle) interactions and, as such, can only be properly treated by including both one-body *and* two-body potentials.[7] Thus, while the experimental mapping of the Fermi momentum allows us to estimate the accuracy of the band-structure calculations, the experimental mapping of the Fermi velocity is of great importance in going beyond the one-electron approximation to determine the effects of the many-body interactions.

In Sec. II, we review the mathematical machinery used to determine the Fermi radius, Fermi velocity, and g factor from the dHvA data. In Sec. III, we discuss the technique needed to specify the orientation of the dHvA samples. The band structure and Fermi surface of Pt are treated in Sec. IV, while experimental techniques and sample preparation are discussed in Secs. V and VI, respectively. Finally the experimental results are presented in Sec. VII.

II. dHvA AND INVERSION THEORY

The dHvA effect is the oscillatory field dependence of the magnetization of single crystals of metals and alloys. This effect is usually only observed in large magnetic fields (greater than 10 kG) and at relatively low temperatures (lower than 2°K). Information about the Fermi surface follows from the Onsager relation[8]

$$F_i = (\hbar c/2\pi e) A_i, \tag{1a}$$

which connects the ith frequency component F_i of the oscillatory magnetization with the corresponding extremal cross sectional area A_i (of the Fermi surface) in planes normal to the field. A full quantitative theory of the dHvA effect has been given by Lifshitz and Kosevich,[9] who find that each extremal cross-sectional area normal to the applied magnetic field contributes a component to the oscillatory magnetization given approximately by

$$\mathbf{M} = \hat{M}_i \left(\frac{e}{hc}\right)^{1/2} \frac{A_i k T}{\pi H^{1/2} (\partial^2 A_i/\partial k_H^2)^{1/2}} \times \frac{\exp(-2\pi^2 c k T_x m_i^*/\hbar e H)}{\sinh(2\pi^2 c k T m_i^*/\hbar e H)} \times \sin[2\pi F_i/H + \beta_i] \cos[\pi g_i m_i^*/2m_0], \tag{1b}$$

where the vector direction of the magnetization is given by

$$\hat{M} = \hat{H} + A_i^{-1}(\partial A_i/\partial\theta)\hat{\theta} + (A_i \sin\theta)^{-1}(\partial A_i/\partial\varphi)\hat{\varphi}.$$

The amplitude of the magnetization oscillations depends on the energy spacing of the Landau levels $\hbar\omega_c$, where the cyclotron frequency is

$$\omega_c = eH/m_i^* c \tag{1c}$$

and the effective cyclotron mass is given by

$$m_i^* = (2\pi)^{-1}(\partial A_i/\partial E). \tag{1d}$$

The Dingle-Robinson temperature T_x results from a broadening of the Landau levels due to collisions and is related to the effective electron scattering time through

$T_x=\hbar/\pi k\tau$. The g factor will be discussed later in this section.

The extremal area A_i of the Fermi surface follows from the determination of the frequency of the dHvA oscillations as the magnetic field is varied in magnitude. Very accurate determinations of the change in extremal area with field direction can then be obtained by changing the field direction while holding its magnitude constant and observing the change in phase of the dHvA oscillations. The effective cyclotron mass $(1/2\pi)(\partial A_i/\partial E)$ follows from the temperature dependence of the amplitude of the dHvA oscillations at fixed field. Once the effective cyclotron mass is known, the scattering time τ follows from the magnetic field dependence of the amplitude of the dHvA oscillations at fixed temperature. The determination of the orbital g factor (or spin mass $m_s/m_0\equiv 2/g$) is, in general, much more difficult than the above measurements. However, if for some special field directions $m^*/m_s=r+\frac{1}{2}$ (where r is an integer) then the fundamental frequency component of the dHvA oscillations will be identically zero, independent of field strength [see Eq. (1)]. We can then determine the spin mass for this angle from a knowledge of the effective cyclotron mass at this angle. If sample purity permitted, one could determine the g factor at all angles by observing the oscillatory behavior at very low temperatures and very high magnetic fields where $\hbar\omega_c\gg kT$ and $\omega_c\tau\gg 1$. In this limit the oscillatory behavior is "spikelike" rather than sinusoidal in character and the spin splitting of the Landau levels is clearly observable. Absolute amplitude measurements would also, in principle, allow a determination of the g factor but are quite difficult to carry out reliably in practice. Thus the angular dependence of the following four quantities of physical interest may be determined from the dHvA effect: (1) $A_i(\theta,\varphi)$, (2) $[\partial A_i(\theta,\varphi)/\partial E]_{\theta,\varphi}$ or equivalently $m_i^*(\theta,\varphi)$, (3) $\tau_i(\theta,\varphi)$, and (4) $g_i(\theta,\varphi)$ or equivalently $m_{si}(\theta,\varphi)$, where again the subscript i refers to the ith extremal orbit on the Fermi surface. All of the above are in some sense averages around an orbit of more fundamental quantities. We will now discuss methods of deriving these more fundamental quantities.

We consider first the area $A(\theta,\varphi)$. The question naturally arises as to whether one can find the radius vector $p(\theta,\varphi)$ from a knowledge of $A(\theta,\varphi)$. Lifshitz and Pogorelov[10] proved that the radius vector $p(\theta,\varphi)$ could be uniquely determined from a complete knowledge of the equatorial area $A(\theta,\varphi)$ provided certain conditions were satisfied. The surface in question must (a) have inversion symmetry, i.e., $A(\theta,\varphi)$ is the equatorial area, (b) have a single-valued radius vector as measured from the center of symmetry. The Lifshitz-Pogorelov expression for the radius vector $p(\theta,\varphi)$ of the surface involves integrations on the area $A(\theta,\varphi)$. In practice the theorem is difficult to apply since the area is known only along various great circles of the unit sphere. Mueller[11] has developed a series-expansion version of the Lifshitz-Pogorelov theorem which overcomes the difficulty. The identity of these two schemes was recently demonstrated by Foldy.[12] We expand the square of the radius vector $p^2(\theta,\varphi)$ and the area $A(\theta,\varphi)$ in the form

$$A(\theta,\varphi)=\sum_{l,m} a_{l,m}Y_{l,m}(\theta,\varphi), \tag{2a}$$

$$p^2(\theta,\varphi)=\sum_{l,m} b_{l,m}Y_{l,m}(\theta,\varphi), \tag{2b}$$

where the a's and b's are expansion coefficients and the $Y_{l,m}(\theta,\varphi)$ are (normalized) spherical harmonics. Mueller's theorem states that

$$a_{l,m}=b_{l,m}\pi P_l(0), \tag{2c}$$

where $P_l(0)$ is the Legendre polynomial of order l. Uniqueness demands that only even l be allowed since $P_l(0)=0$ for odd l; this is equivalent to requiring inversion symmetry. The $a_{l,m}$ are determined by least-squares fitting the experimental data to expression (2a) to some order L, the corresponding radii following immediately from (2b) and (2c). The magnitude of L is determined by a number of factors. Firstly, the value of L should be high enough to give an adequate representation of the true surface. If the true surface has a radius that varies considerably over relatively small angular ranges, a relatively high value of L will be required. Secondly, the question of how extensive a given set of data must be in order to reliably determine the higher-order coefficients is an important one. dHvA data are only observed in planes in which the magnetic field is rotated. Mueller and Priestley[13] demonstrated that if (continuous) data are available only in the (100) and (110) planes, as is usually the case for surfaces having cubic symmetry, then the fit must be limited to 11 terms ($L=18$). Since the anisotropy of the surfaces observed in this investigation required higher L values for a faithful representation, additional data off of symmetry planes was clearly required. The choice of optimal great circles on which to take data is at present unclear. However, since the samples used in these experiments were randomly grown (but not oriented) the choice is already somewhat restricted. We adopted the rather severe restriction that there be no point in the basic triangle ($\frac{1}{48}$ of the unit sphere for full cubic symmetry) that was more than 3° away from a great circle on which data had been taken. More will be said on this matter in Sec. IV.

We now discuss the effect of a symmetry higher than that governed only by the inversion operator on the expansions (2a) and (2b). The inclusion of additional symmetry operations restricts the values of m that can occur and also, in the case of cubic symmetry, results in relationships among the expansion coefficients.

The cubic case (the group O_h) has been considered in detail (to order $L=30$) by Mueller and Priestley,[13] and (to order $L=60$) by Aurbach *et al.*[14] New harmonics K_{il} (called Kubic harmonics) are defined which are

related to the real spherical harmonics C_{lm} by the relation

$$K_{il}=\sum_m a_{ilm}C_{lm}, \tag{2d}$$

where the coefficients a_{ilm} are given in Refs. 11 and 14. The C_{lm} are related to the usual complex spherical harmonics by $C_{lm}=1/\sqrt{2}(Y_{l,m}+Y_{l,-m})$ and $C_{l0}=Y_{l,0}$. The area inversion theorem then takes the following form:

$$A(\theta,\varphi)=\sum_{il}\beta_{il}K_{il}(\theta,\varphi), \tag{3a}$$

$$p^2(\theta,\varphi)=\sum_{il}\gamma_{il}K_{il}(\theta,\varphi), \tag{3b}$$

$$\beta_{il}=\pi P_l(0)\gamma_{il}, \tag{3c}$$

where β_{il} and γ_{il} are the expansion coefficients of the area and radius, respectively.

We now turn to the effective mass $m^*=1/2\pi(\partial A/\partial E)_{\theta,\varphi}$. It is easy to show that by combining effective-mass measurements with area measurements one can determine the Fermi velocity.[15] The Fermi velocity is defined as[7]

$$\begin{aligned}\mathbf{v}=\nabla_p E(p)&=(\partial E/\partial p)_{\theta,\varphi}\hat{p}+p^{-1}(\partial E/\partial\theta)_{p,\varphi}\hat{\theta}\\&\quad+(p\sin\theta)^{-1}(\partial E/\partial\varphi)_{p,\theta}\hat{\varphi}\\&=v_p\hat{p}+v_\theta\hat{\theta}+v_\varphi\hat{\varphi}.\end{aligned} \tag{3d}$$

We make the expansion (for cubic symmetry)

$$(\partial A/\partial E)_{\theta,\varphi}=\sum_{il}\beta_{il}'K_{il}(\theta,\varphi), \tag{4a}$$

where the β_{il}' are the expansion coefficients. From our previous discussion we then have

$$(\partial/\partial E)[p^2(\theta,\varphi)]=2p(\partial p/\partial E)_{\theta,\varphi}=\sum_{il}\gamma_{il}'K_{il}(\theta,\varphi), \tag{4b}$$

where $\beta_{il}'=\pi P_l(0)\gamma_{il}'$. Combining this with (3b) we have immediately the $\hat{p}$ component of the Fermi velocity:

$$v_p=2[\textstyle\sum_{il}\gamma_{il}K_{il}(\theta,\varphi)]^{1/2}/\sum_{il}\gamma_{il}'K_{il}(\theta,\varphi). \tag{5a}$$

The $\hat{\theta}$ and $\hat{\varphi}$ components of the velocity follow from using the relations

$$\left(\frac{\partial E}{\partial\theta}\right)_{p,\varphi}=-\left(\frac{\partial p}{\partial\theta}\right)_{E,\varphi}\Big/\left(\frac{\partial p}{\partial E}\right)_{\theta,\varphi}$$

and

$$\left(\frac{\partial E}{\partial\varphi}\right)_{p,\theta}=-\left(\frac{\partial p}{\partial\varphi}\right)_{E,\theta}\Big/\left(\frac{\partial p}{\partial E}\right)_{\varphi,\theta},$$

with which we obtain

$$v_\theta=\frac{-\sum_{il}\gamma_{il}(\partial/\partial\theta)K_{il}(\theta,\varphi)}{[\sum_{il}\gamma_{il}'K_{il}(\theta,\varphi)][\sum_{il}\gamma_{il}K_{il}(\theta,\varphi)]^{1/2}}, \tag{5b}$$

$$v_\varphi=\frac{-\sum_{il}\gamma_{il}(\partial/\partial\varphi)K_{il}(\theta,\varphi)}{\sin\theta[\sum_{il}\gamma_{il}'K_{il}(\theta,\varphi)][\sum_{il}\gamma_{il}K_{il}(\theta,\varphi)]^{1/2}}. \tag{5c}$$

Complete knowledge of $p(\varphi,\theta)$ allows us to determine the volume in momentum space occupied by electrons (or unoccupied for holes) within a given sheet of the Fermi surface. The number of states $n(E)$ (electrons or holes) is of course $[2/(2\pi\hbar)^3]\times$volume. Thus we have

$$n(E)=\frac{2}{3(2\pi\hbar)^3}\int_0^{2\pi}\int_0^{\pi}p^3(E,\theta,\varphi)\sin\theta\,d\theta d\varphi. \tag{6}$$

Complete knowledge of $p(\theta,\varphi)$ and $\mathbf{v}(\theta,\varphi)$ allows a determination of the density of states, where $N(E)=\partial n(E)/\partial E$. Differentiating Eq. (6) with respect to E and using the definition of v_p we obtain

$$N(E)=\frac{2}{(2\pi\hbar)^3}\int_0^{2\pi}\int_0^{\pi}\frac{p^2(E,\theta,\varphi)\sin\theta\,d\theta d\varphi}{v_p(E,\theta,\varphi)}. \tag{7}$$

Knowledge of the number of carriers allows verification of many-body theories relating to the conservation of quasiparticle states, in particular, charge neutrality for a metal of even valence such as Pt.[16] If the density of states is known for all sheets of the surface we may compare it with the heat capacity. These two should be in agreement according to the Landau quasiparticle theory.[7] The average many-body enhancement follows on comparison with the band-structure density of states.

The above inversion techniques are suitable for the Γ-centered surface of Pt (to be discussed later) since it is a closed, single-valued surface of full cubic symmetry. The representation and inversion of surfaces having lower symmetry has been treated by the authors.[17] The X-centered pocket in Pt has the point-group symmetry D_{4h}, and we choose the fourfold axis as the z axis. The fact that the z axis is a fourfold axis restricts the values of m ($\leq l$) to 0, 4, 8, $\cdots$, i.e., $m=0$ (mod 4). The expansion takes the form

$$A(\theta,\varphi)=\sum_{l,m}\beta_{l,m}C_{lm}, \tag{8a}$$

$$p^2(\theta,\varphi)=\sum_{l,m}\gamma_{lm}C_{lm}(\theta,\varphi), \tag{8b}$$

$$\beta_{il}=\pi P_l(0)\gamma_{il}, \tag{8c}$$

where the C_{lm} were defined previously. A problem arises in applying the inversion procedure to ellipsoids. The expansions (8a) and (8b) do not in general terminate after a finite number of terms and thus the accurate specification of an ellipsoid requires a large number of terms. On the other hand, we know that an ellipsoid of revolution (appropriate to the X-centered holes) requires only two terms for a complete specification. By rescaling the principal axis one may map the ellipsoid into a sphere and thus the expansions (8a) and (8b) terminate after the first term. We define the transformation $p_x'=p_x$, $p_y'=p_y$, $p_z'=\gamma p_z$ and refer to this transformation as a spherical mapping. It has been shown[17] that the behavior of the area and radii under

this spherical mapping is given by

$$A'(T^{-1}\theta,\varphi)=[\gamma^2+(1-\gamma^2)\cos^2\theta]^{1/2}A(\theta,\varphi), \quad (9a)$$

$$p'^2(T\theta,\varphi)=[1+(\gamma^2-1)\cos^2\theta]p^2(\theta,\varphi), \quad (9b)$$

where the transformed angles $T\theta$ and $T^{-1}\theta$ are given by

$$T\theta=\tan^{-1}(\tan\theta/\gamma), \quad (10a)$$

$$T^{-1}\theta=\tan^{-1}(\gamma\tan\theta). \quad (10b)$$

Equations (9) and (10) apply only to the case of an ellipsoid of revolution. The general case is slightly more complicated (see Ref. 17). The fitting procedure is as follows. The experimental areas are first transformed into the primed system with the aid of Eq. (9a). The primed areas are then least-squares fitted to (8a) to some order ($l=2$–6 in our case). The radii in the primed system are obtained using (8c) and then transformed to the lab system using Eq. (9b). This completes the inversion. This procedure is not essential in Pt, where the surfaces are ellipsoidal to a high degree of accuracy, but is of great importance in materials such as Sb and As. Nonetheless the computer programs were available and have been applied to Pt as will be discussed later in this paper.

So far we have considered surfaces invariant under various point-group operations, and spherical harmonics are an appropriate representation for such surfaces. The other major sheet of the Fermi surface of Pt is multiply connected (open). The proper treatment of an open surface requires a representation which is invariant under the operations of the space group. A three-dimensional Fourier series of the form

$$E(\mathbf{k})=\sum_{\mathrm{R}} C_{\mathrm{R}}\exp(i\mathbf{k}\cdot\mathbf{R}) \quad (11)$$

is a suitable representation which includes the full space-group symmetry. This representation has been used by Roaf[18] and Halse[19] to invert the dHvA data in the noble metals. Ketterson, Mueller, and Windmiller[20] have recently shown that this representation can also accurately represent the highly distorted constant-energy surfaces of Pt. The procedure used was to least-squares fit values of $E(\mathbf{k})$ in the neighborhood of the Fermi energy (determined by the band-structure calculation of Mueller, Ketterson, Windmiller, and Hörnfeldt[5]) to Eq. (11). Using these coefficients the anisotropy of the area for all the orbits in Pt was calculated and shown to be in satisfactory agreement with the data to be presented in this paper. A rapidly converging inversion procedure was also developed but has not yet been applied. The application of this new inversion technique and its extension to include inversion of effective mass and pressure-dependence data will be the subject of a separate paper.[21]

We should also mention that one may use a parametrized band-structure program to convert dHvA areas into Fermi-surface radii, thus getting a band structure in the process. One varies the band-structure parameters until a best fit is obtained between the experimental areas and those calculated from the band structure. The pseudopotential approach does not presently work well for transition metals. The potential used in a KKR or APW approach, however, may be parametrized via phase shifts, and this approach looks very promising. The interpolation scheme has also been applied to Pt.[5]

The $\tau(\theta,\varphi)$ measured in a dHvA effect is an orbital average of the point relaxation time. An inversion theory for $\tau(\theta,\varphi)$ has not been given to date but this may be an important area for future investigation.

Recently we suggested that a geometrical interpretation could be given to the electronic g factor in a metal.[22] The magnetic moment associated with the electronic spin angular momentum $\mathbf{S}$ causes each Landau level to be split into two levels separated by an energy $\Delta E=2\boldsymbol{\mu}\cdot\mathbf{H}$ where $\boldsymbol{\mu}=g(\theta,\varphi)(e\hbar/2m_0c)\mathbf{S}$. If there were no spin-orbit coupling (or many-body effects) the g factor would have the free-electron value of 2. We expand ΔE of a specific Landau level n in a power series to first order:

$$\Delta E=[(\partial E_{\downarrow}/\partial H)_n-(\partial E_{\uparrow}/\partial H)_n]H+\cdots,$$

where $E_{\uparrow}$ is the energy of a state whose spin is largely up and $E_{\downarrow}$ is the corresponding state whose spin is largely down.

Through a band structure we have $A=A(E)$ and from the Onsager relation we have $A=A(n,H)=(2\pi e\hbar H/c)(n+\gamma)$. Using the chain rule $(\partial E/\partial H)_n=(dE/dA)(\partial A/\partial H)_n$, the magnetic moment becomes

$$\mu=e\hbar/2m_s(\theta,\varphi)c$$
$$=[4\pi m^*(\theta,\varphi)]^{-1}[A_{\uparrow}(\theta,\varphi)-A_{\downarrow}(\theta,\varphi)/H]. \quad (12)$$

Equation (12) gives us the desired geometrical interpretation of the g factor (or equivalently the spin mass). Under the assumption (probably unjustified) that each point on the Fermi surface is displaced by the same amount for a given external field regardless of the direction of the field, we could formally use the velocity-inversion techniques to determine $\partial p/\partial H$. With this information we could determine the change in volume with field which is proportional to the magnetic susceptibility for that sheet of the surface. The way in which many-body effects enter the g factor is not understood at present.

III. SAMPLE-ORIENTATION THEORY

In this section we describe the techniques used to specify and orient the samples. As mentioned in Sec. II, it is necessary to take data off of symmetry planes if the coefficients of the higher spherical harmonics are to be determined accurately. Now a harmonic of order L changes sign as θ changes by an amount $\Delta\theta=180°/L$, or 6° for $L=30$. It would be desirable to have the sample orientation known to about 20 times this accuracy or ~0.3°. Using x-ray techniques it is difficult to orient a

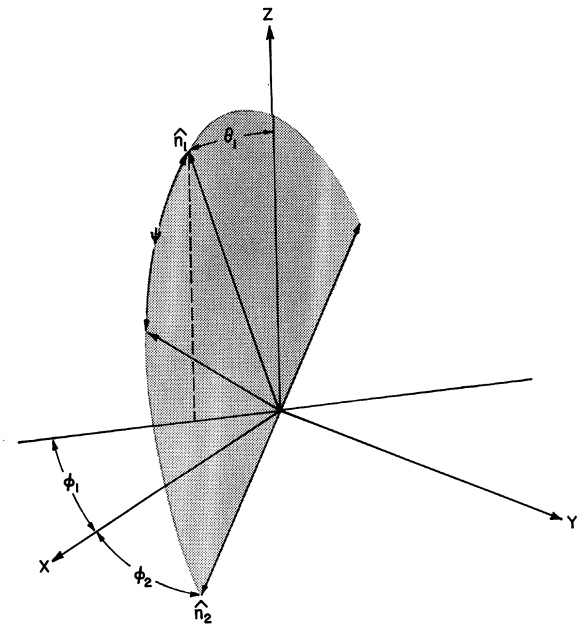

FIG. 1. Plane of rotation of the sample as specified by the vector $\hat{n}_1$ and $\hat{n}_2$ (see text).

sample better than 2°. In order to achieve the necessary orientation accuracy we have developed a technique which makes use of the known crystal symmetry (cubic in this case).[23] As is well known, the specification of a rigid body rotated about an arbitrary axis requires knowledge of three angles. The three Euler angles are a common example but were not the coordinates used here. The coordinates used in this investigation were dictated by the particular sample geometry and are discussed below.

The sample has the shape of a long right-circular cylinder approximately 1 mm in diameter by 5 mm long. A sample rotator positions the sample relative to the solenoid axis or equivalently relative to the magnetic field direction. The sample axis is specified by the unit vector $\hat{n}_1$ having polar angles θ_1 and φ_1 relative to the crystal axis measured in a right-handed coordinate system as shown in Fig. 1. θ_1 is the polar angle from the sample axis to the nearest [001] crystal axis (called the z axis). φ_1 is the azimuthal angle of the sample axis measured from one of the other two remaining [100] axes (called the x axis). This completes the specification of the sample axis. To define a plane of rotation of a sample we must specify another vector $\hat{n}_2$ not collinear with $\hat{n}_1$. The choice of the second vector is somewhat arbitrary since any two (noncollinear) vectors are sufficient to define the plane of rotation. We chose the second vector $\hat{n}_2$ as the intersection of the plane of rotation of the magnetic field with the xy plane of the crystal, (the y axis being the third [010] axis). θ_2 and φ_2 are the polar coordinates of this vector, where θ_2 is obviously 90°. The angle φ_2 is, however, nonunique since the crystal xy plane and the plane of rotation of the sample intersect at two values of φ_2, one being 180° greater than the other. The specification is made unique in the following way. We denote the experimental angle of the sample rotator as ψ. The second vector (xy plane intersection vector) is chosen in the direction of *increasing* values of ψ as the sample axis is turned away from the magnet axis. This then defines φ_2. The determination of the zero of the experimental angle ψ is accomplished by observing the disappearance of the inductive pickup when the pickup coil (sample axis) is perpendicular to the vertical modulation coil axis (magnet axis). The calibration constant of the angle ψ (number of experimental dial divisions per degree) is found by observing the number of dial divisions between the two null points at $\psi=\pm 90°$.

Now it was usually observed that the dHvA frequency was not quite reproducible when the sample was rotated by 180°, and the difference was well outside experimental error. Crystal symmetry demands that the frequency be invariant under such a rotation if we are truly rotating the magnetic field in a plane (on a great circle) relative to the crystal. The fact that the frequency is not reproducible is clear evidence that the sample rotator is not rotating the sample exactly in a plane. The magnitude of the effect could be explained if it was assumed that instead of rotating on a great circle (plane) the sample was actually rotating (approximately) on a cone of half-angle $\alpha=90°\pm\sim\frac{1}{2}°$. The angle α is defined so that it is less than 90° in the hemisphere intersecting the vector $\hat{n}_1\times\hat{n}_2$. A short calculation showed that this was not unreasonable since a clearance of the order of a thousandth of an inch in the rotor bearings of the sample rotator could account for the effect. Also the magnet and sample rotator might easily be tilted (in an arbitrary plane) with respect to each other by this amount. It was clear that our orientation procedure would have to include this effect.

The change of the dHvA frequency with angle ψ is determined from a field rotation. To determine the absolute frequency it is necessary to make at least one magnetic field sweep (although in practice this was done at least every 10°). Whereas the change in frequency with angle may be determined to about a part in 10^5 for a frequency of $\sim 10^9$ G, the absolute frequency from a field sweep can be determined to only about a part in 10^3. Thus in comparing equivalent points in one plane of data with another the absolute frequencies may be in error by about 0.1%. In doing accurate work it is necessary to include an additive correction for the data in one plane relative to another. This additive constant A_0 was also determined from the data. We thus have five parameters to determine: A_0, θ_1, φ_1, φ_2, and α. θ_1, φ_1, and φ_2 can be approximately determined ($\pm 2°$) from x rays. We have developed a variation procedure for improving the accuracy of θ_1, φ_1, and φ_2

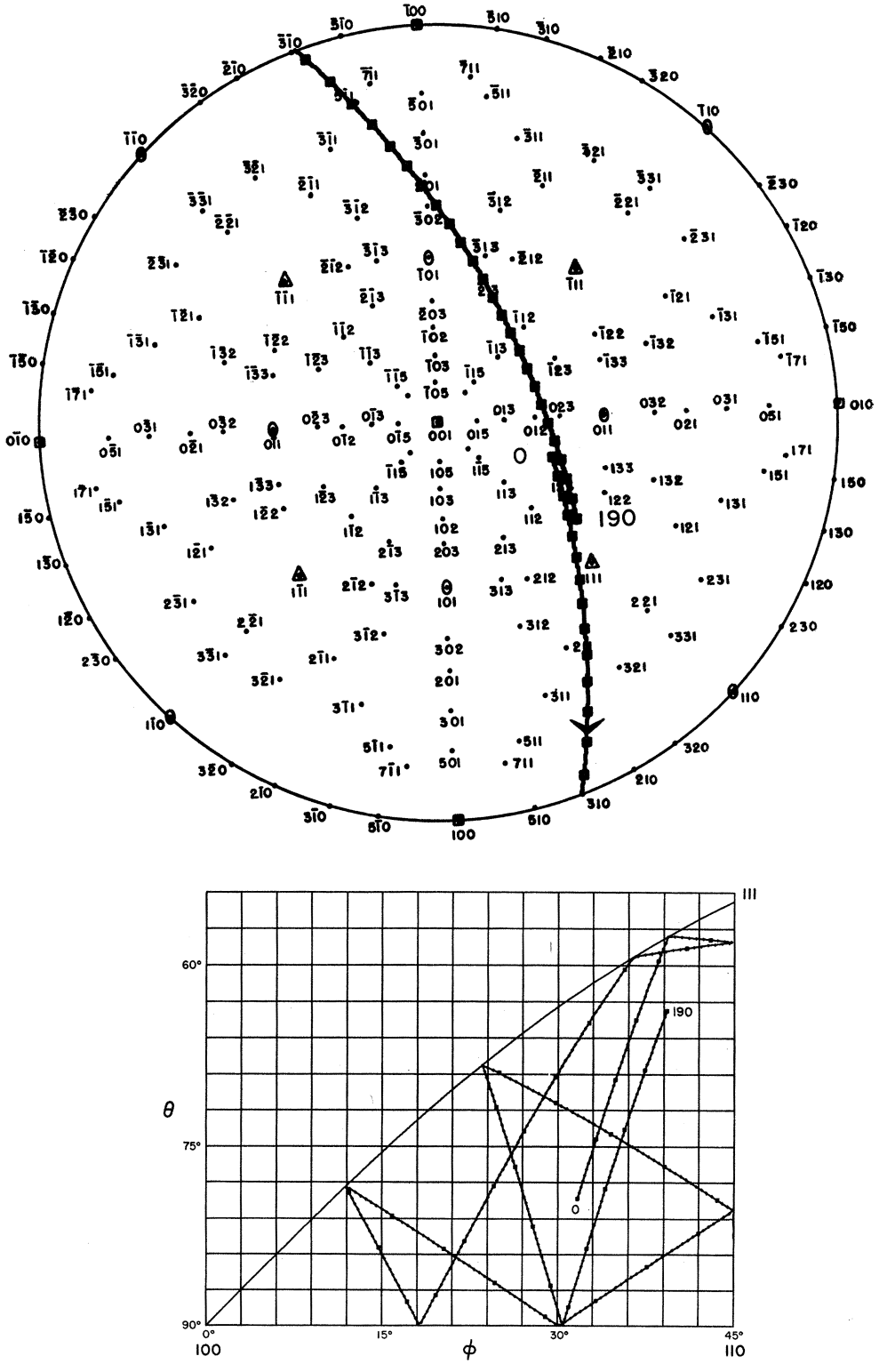

FIG. 2. (a) Stereographic plot of the plane (cone) of rotation of run *g*. (b) Plane (cone) of rotation of the magnetic field for run *g* in the basic 1/48th of the unit sphere.

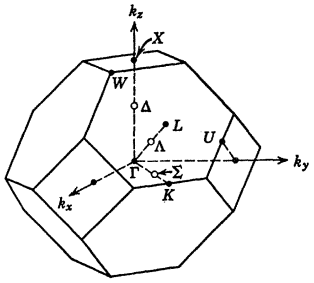

FIG. 3. Brillouin zone for fcc crystal structure.

and for determining α, all to order 0.2°, by using the cubic symmetry of the data.[23] This procedure is outlined below.

The solid line in Fig. 2(a) shows, on a sterogram, one of the "planes" on which data were taken (the final values of the four parameters θ_1, φ_1, φ_2, and α were used in this plot). Figure 2(b) shows the same data (on mercator projection) where now we have confined the angles θ, φ to be in the basic 1/48th of the unit sphere by performing the required symmetry operations. Observe that the contour on which the data were taken intersects itself seven times. An intersection point corresponds to a pair of experimental angles ψ_1 and ψ_2. The experimental dHvA frequencies at these angles must then necessarily be the same because of the cubic symmetry. This suggests using these "intersections" to orient the sample since there are in general seven intersections and only four orientation parameters. What one does is assume some initial orientation parameters and then vary the parameters until the sum of the squares of the differences between the experimental areas at the intersection angles is a minimum. In addition to the intersections of a given plane of data with itself we may also consider the intersection of two or more planes with each other. Two arbitrary planes will in general intersect each other 22 times, so that we get much more redundancy and thus greater accuracy by considering more than one plane. A computer program was developed which carried out the orientation automatically. A value of A_0 is also determined when comparing the orientation of two planes. We refer the reader to Ref. 23 for the details.

IV. BAND STRUCTURE AND FERMI SURFACE OF Pt

Figure 3 shows the Brillouin zone for the fcc structure. The band structure of Pt has been calculated, using the RAPW technique, by Andersen and Mackintosh.[4,24] Their band structure is shown in Figs. 4(a) and 4(b). Figure 4(a) shows the band structure along the principal symmetry lines of the Brillouin zone. Note that there are six levels which arise from the atomic s and d states. Figure 4(b) shows the Δ line (Γ to X) with and without relativistic effects (such as spin-orbit coupling). For a nonrelativistic band structure the level Δ_5 is doubly degenerate. This degeneracy, if not lifted, leads to an intersecting Fermi surface and thus magnetic breakdown. The inclusion of relativistic effects lifts this degeneracy, splitting the Δ_5 level into the two levels Δ_6 and Δ_7. The dashed line shows the position of the Fermi energy placed from the requirement that the six bands hold exactly five electrons per atom (10 with spin). Three of the six levels cut the Fermi energy and thus the Fermi surface has three distinct sheets (not related by symmetry) containing a total of two electrons per atom (four with spin). One of these surfaces is closed and centered on the point Γ of the Brillouin zone. The extension of this surface in the [100], [110], and [111] directions is the intersections of the Fermi energy with the lines Σ_7, Δ_7, Λ_7 respectively. Were there no hybridization (mixing of s levels with d levels) this surface would have s symmetry, and it has become customary to refer to this surface as the s-band surface. The degree of hybridization is, however, considerable so that this designation is inappropriate. We will refer to this surface simply as the Γ-centered surface. Since the states within this surface are occupied, it is an electron surface. A drawing of this surface (as determined from the calculation of Mueller *et al.*[5]) is shown in Fig. 5(a).

From Fig. 4(b) we see that the next-to-highest Δ_6 level cuts just above the Fermi energy near the point X. This level, X_{6+}, which lies above the Fermi energy at X, drops below the Fermi level in moving away from the point X in any direction. It is thus more convenient to think in terms of the small number of unoccupied or hole states when considering the surface associated with this pocket. Since we are very near the band extremum the band structure is nearly parabolic and the surface is approximately an ellipsoid of revolution about the Γ-X line. The X-Γ extension of this surface is

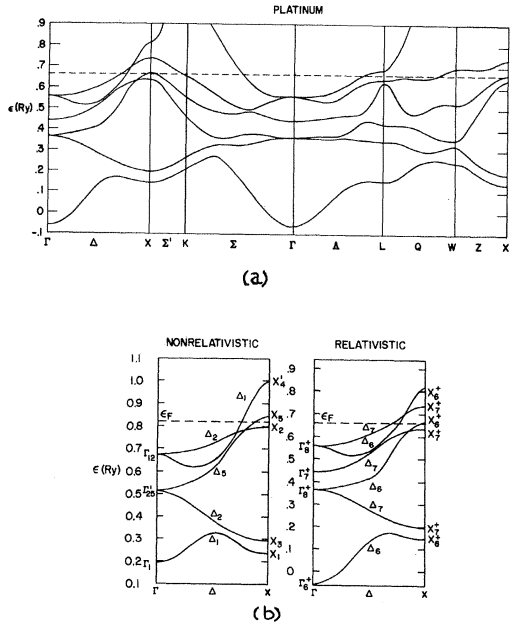

FIG. 4. (a) Energy-band structure of Pt along the principal symmetry lines of the Brillouin zone as calculated by Andersen and Mackintosh using the RAPW technique. (b) Energy-band structure along the Δ line with and without relativistic effects.

approximately $1\frac{1}{2}$ times greater than the X-U or X-W extension. This surface will be referred to as the pocket.

The third sheet of the Fermi surface of Pt is associated with the level X_{7+}. This surface is also most conveniently interpreted as a hole surface. Referral to Fig. 4(a) shows that this (hole) surface is open in the X-W direction but closed in the X-Γ and X-U directions [the band structure in the X–U direction is the same as the X-K or Σ' line shown in Fig. 4(a) by symmetry].

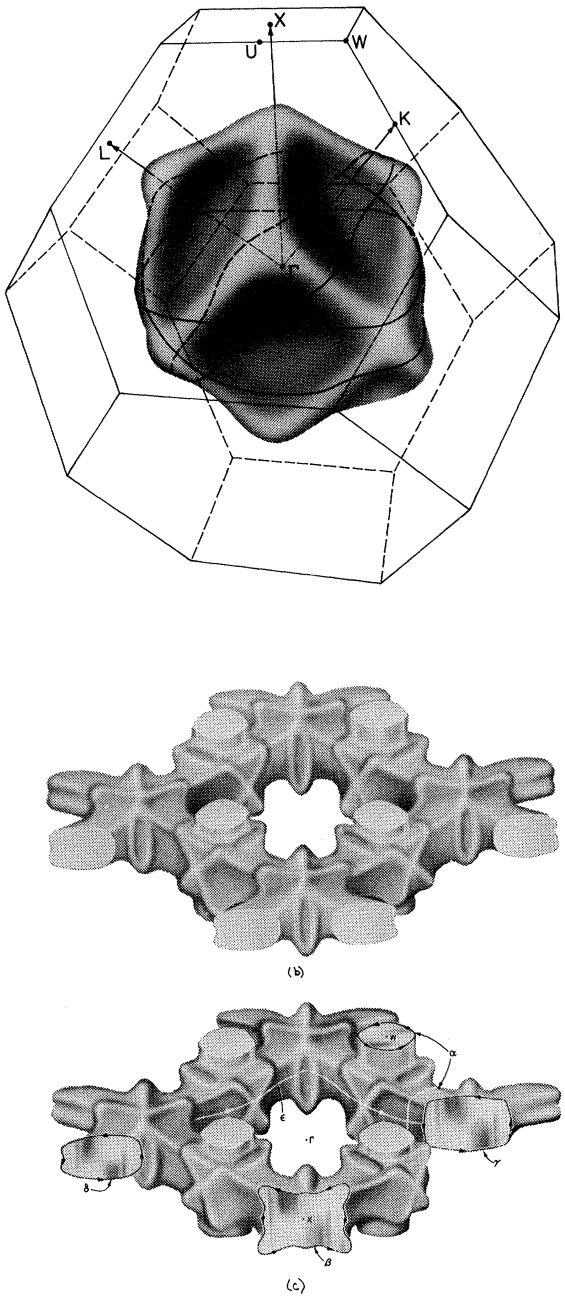

FIG. 5. (a) Electron Fermi surface of Pt. (b) Open sheet of the Fermi surface of Pt showing connectivity, viewed from approximately the ⟨111⟩ direction. (c) Cutaway of the open sheet of the Fermi surface of Pt showing the α, β, γ, and δ orbits (in a magnetic field).

The X-Γ extension is given by the intersection of the Fermi energy with the Δ_6 line. Note that the Γ-centered electron and this open surface do not contact each other as the intersecting of the levels Δ_6 and Δ_7 would seem to indicate since this degeneracy is lifted as we move off the Δ line. In the repeated zone scheme this surface has the connectivity of cylinders extending in the [100] directions and intersecting in pairs at the points X. A drawing of this surface (as calculated by Mueller *et al.*[5]) is shown in Figs. 5(b) and 5(c). This surface will be referred to as the open surface.

Since two of the sheets were interpreted as holes and the volume of all three levels cutting the Fermi energy must contain two electrons, it follows that the total volume in the open surface and the three pockets must equal the volume of the Γ-centered electron surface.

Preliminary studies of the dHvA effect[25–30] have verified the existence of all three sheets of the Pt Fermi surface. The topology and approximate dimensions were shown to be in agreement with the band-structure calculations.

V. EXPERIMENTAL TECHNIQUE

The details of the experimental techniques used in this investigation have been treated elsewhere.[31,32] The large amplitude, low-frequency field modulation technique was employed. Almost all of the known techniques for enhancing specific dHvA frequencies were used at one time or another in this investigation. These include (a) nulling an undesired frequency by angular modulation, (b) enhancing higher-frequency dHvA oscillations by detection at a high harmonic of the modulation frequency, (c) nulling an undesired frequency at a "Bessel function zero," and (d) sweeping the magnetic field proportional to $1/t$ while time filtering to enhance a desired frequency.

Magnetic fields were produced by a $1\frac{1}{2}$-in.-bore 60-kG Varian[33] superconducting solenoid. Since the insert Dewar had a bore of $\frac{5}{8}$ in. (at its lower extremity) this left the remaining annulus for the modulation coils. Both longitudinal and transverse modulation coils were contained in this annulus. By controlling the current in the longitudinal and transverse coils the modulation angle could be adjusted. In later measurements it was judged advantageous to give up the transverse modulation capability in order to have greater magnetic field capability. The transverse modulation coil was removed and the considerable space thus made available was filled by an insert superconducting solenoid made of NbTi wire which was energized in series with the main coil. The composite reached a maximum field of 72 kG. Both the main magnet and the composite system were calibrated with NMR.

Since the dHvA amplitude increases greatly on going to lower temperature [see Eq. (1)], the system was designed to allow evaporative cooling of the sample with either He^4 or He^3. The experimental Dewar contained two separate regions: an annulus containing He^4 (in the upper region of the Dewar above the magnet) and an

inner tube which contained the sample rotator and sample together with the He^3 or He^4 used to cool the sample. This inner tube was in contact with the He^4 annulus in the upper region of the Dewar (so that the liquid could be condensed) and isolated from the magnet helium bath by a vacuum space in the lower portion of the Dewar. When He^3 was used, temperatures as low as 0.35°K were achieved.

Superfluid He^4 was usually used in the inner tube (because of its very high thermal conductivity) for studies of the temperature (and field) dependence of the dHvA amplitude in order to determine the effective cyclotron mass (and Dingle temperature). In the superfluid regime, the temperature of both He^4 reservoirs will be the same provided that the liquid level in the inner tube does not extend up too high. The sample temperature could then be adjusted by pumping on the outer annulus while accurate temperature determinations were achieved by measuring the vapor pressure in the inner tube with a Texas Instruments precision pressure gauge.[34] In this way the temperature uncertainties due to pressure drop in a pumped line were eliminated while those due to thermomolecular pressure corrections were kept negligible through the use of a sufficiently large diameter inner tube. Less accurate cyclotron effective-mass measurements are obtained when using He^3 (because of the poorer thermal conductivity) in the inner tube. For this case, the temperature is adjusted by pumping on the He^3. Precautions are necessary to ensure that the pressure is not reduced to the point where uncertainties in the pressure drop through the pumped line result in significant errors in the temperature determination.

The sample rotator[32] was precision machined from Hysol low-temperature epoxy.[35] When making the differential dHvA frequency measurements, the sample was rotated continuously by an external motor drive system. For certain field directions (near 110) the Γ-centered surface of Pt is sufficiently anisotropic that 80 oscillations per degree are observed for a field of approximately 50 kG. The smoothness with which the sample rotator turned was such that the oscillations during such a field rotation could be easily resolved. He^3 was used when measuring the frequency of the dHvA oscillations in order to have the largest amplitude.

VI. SAMPLE PREPARATION

It is quite important that the samples be both pure and strain free. If the sample is bent by as little as 0.01° it can greatly reduce the dHvA amplitude. Since the process of shaping the sample can introduce strain it was decided to use the sample cross section "as grown" and simply cut it to the right length. All samples were formed from Sigmund Cohn[36] reference grade 1-mm-diam (0.040 in.) platinum wire of nominal 5–9 purity. Suitable samples were made by two different techniques. In the first technique a short length of wire ($\sim 2\frac{3}{4}$ in long) was heated in air to 1400°C (±20°C) (the melting point of Pt is 1769°C) over a zone about $\frac{1}{4}$ in. in length. Heating was accomplished with a water-cooled rf copper concentrator,[37] the concentrator being excited by a 10 kW rf generator. The heated zone was then moved a distance of 1 in. along the wire over a 200-min time interval. Randomly oriented grains up to $\frac{1}{2}$ in. in length resulted in many cases. The larger grains were cut out of the wire with a "moving wire" spark cutter. Grain boundaries were made visible by electrolytically etching the sample.[38] The etch was a 20% solution of HCl and saturated NaCl solution. A 2.0-A ac current was passed between the sample wire and a second Pt wire which served as the other electrode. Samples were etched for approximately $\frac{1}{2}$ h. In the second method of preparation a floating zone refiner employing rf concentrator heating[39,40] was used. The process was carried out in a vacuum of 10^{-7} Torr. A randomly oriented single crystal almost always resulted from a single pass. The zone was passed at a rate of 1 in./h over a length of 1–2 in. and the sample was then parted to avoid straining the sample from thermal contraction on cooling. Samples 4–5 mm in length were cut out with the spark cutter. The resistance ratio of such samples was between two and three thousand. Resistance ratio measurements were not performed on the samples prepared by the first technique but they did give somewhat larger dHvA amplitudes. Air annealing techniques have yielded resistance ratios as high as 7610 in Pt.[41] It was often observed that the dHvA amplitude diminished after the sample was cycled several times between room and helium temperature indicating that temperature cycling introduces some strain. Additional information on the growth of Pt group crystals can be found in Ref. 39.

VII. EXPERIMENTAL RESULTS

A. General

dHvA frequencies were studied for the magnetic field in eight separate nonsymmetry planes. These will be designated by the letters *a* through *h*. Planes *a–c* were all taken on the same sample. This sample was cut from a larger crystal which had been prepared by the annealing technique. Likewise planes *d–f* were also taken on a single specimen, which was cut, however, from a different crystal prepared on a separate annealing run. Specimen *g* was cut from the same crystal as the sample used for runs *d–f*. Specimen *h* was cut from a crystal prepared by the floating zone technique, the reason being that the growth axis for crystals prepared in this manner is often such that it is possible to rotate the sample nearly in a (110) plane. Indeed, run *h* is very nearly in the (110) plane.

Frequencies associated with all three sheets of the surface were observed in all experimental runs. For the Γ-centered surface, oscillations were observed at all angles except where spin-splitting zeros caused the amplitude to vanish. The samples were oriented from the cubic symmetry of this Γ-centered surface data as described in Sec. III.

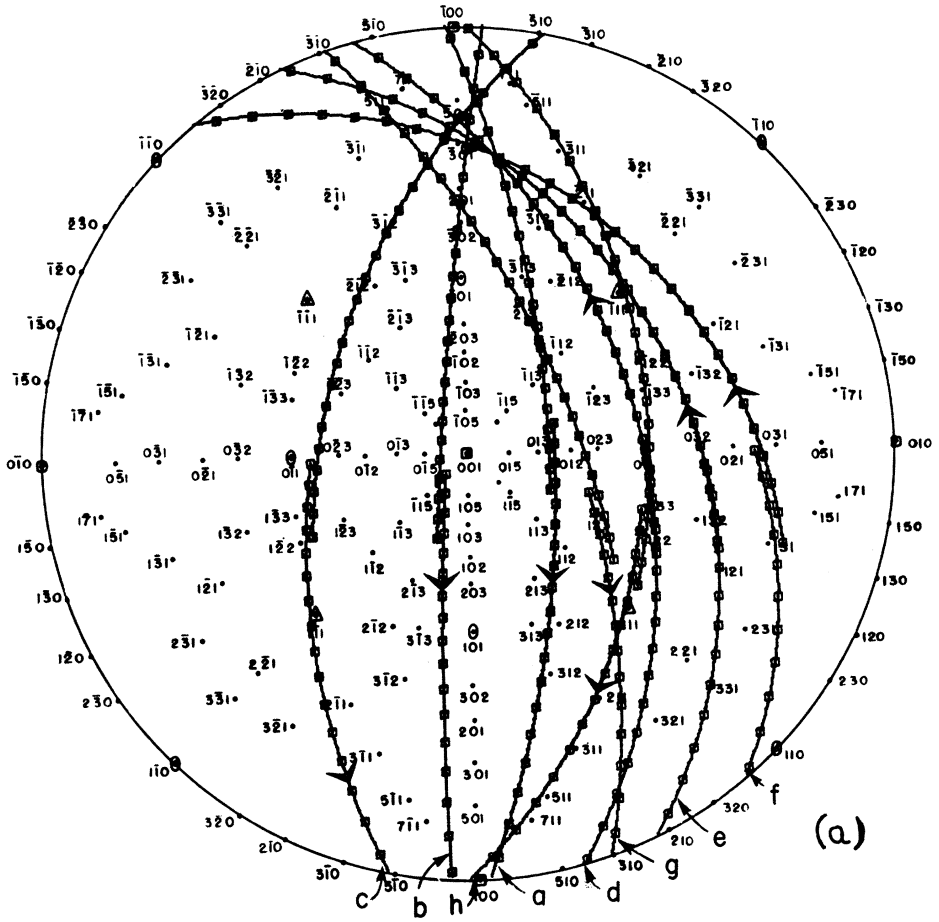

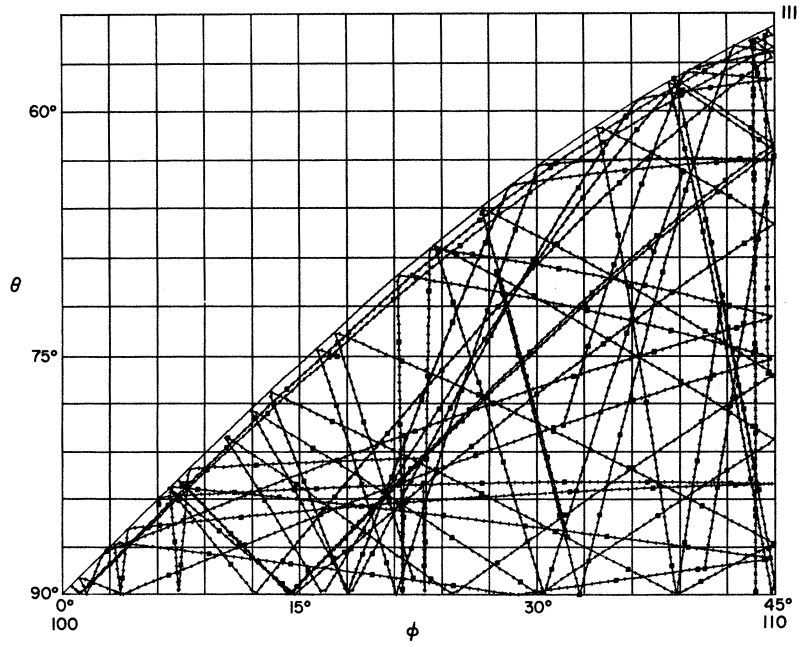

FIG. 6. (a) Stereographic plot of the eight planes (cones) *a–h* in which the dHvA effect was studied in Pt. The units along the traces of the magnetic field correspond to changes of 5 in the experimental coordinate ψ, corresponding to a change in angle of 5.165 degrees. (b) Planes *a–h* folded into the basic 1/48th of the unit sphere.

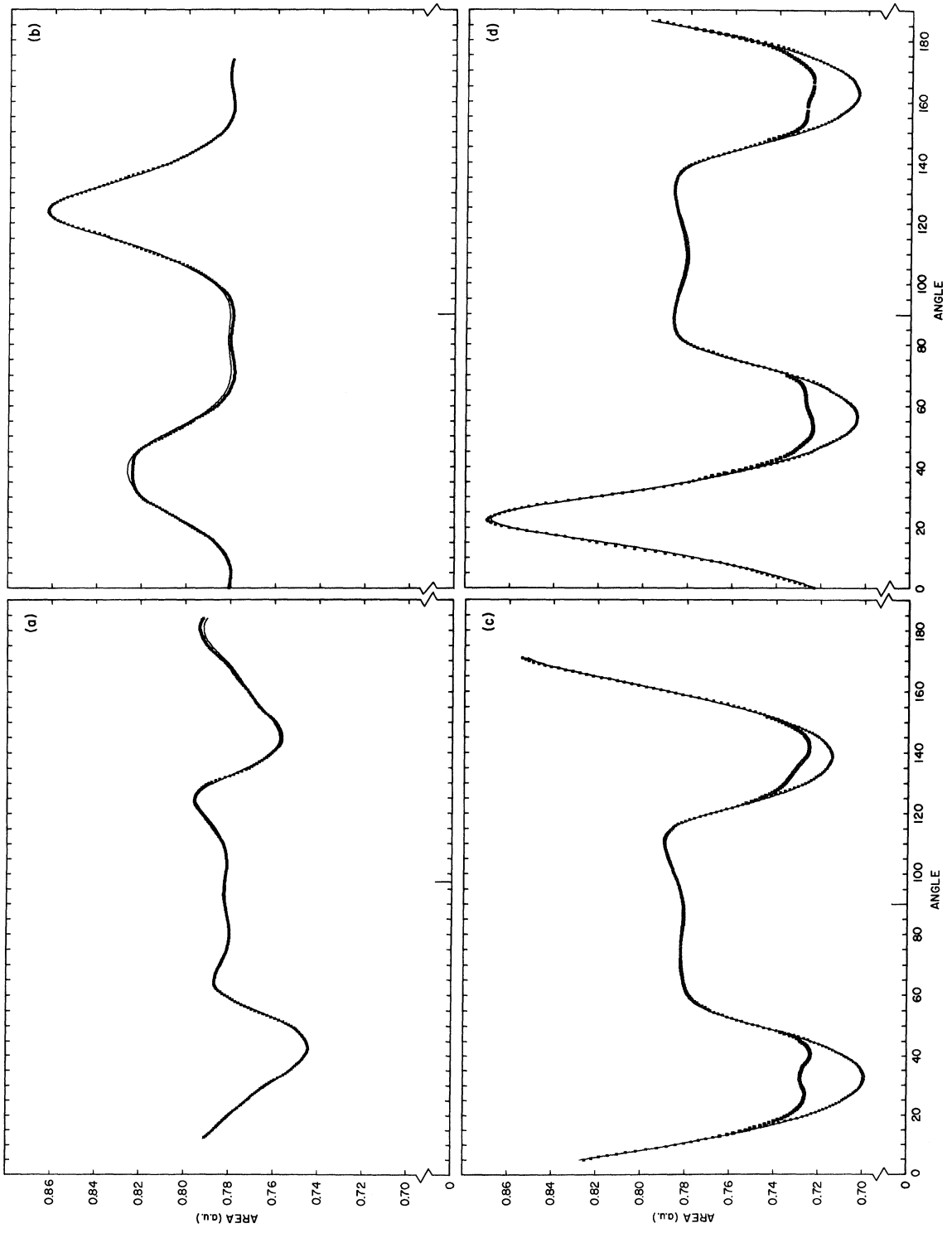

FIG. 7. Angular dependence of the extremal area for the Γ-centered electron surface observed in runs *a–h*. Solid line shows the $L=30$ fit. The angular scale corresponds to the experimental coordinate ψ as shown in Fig. 6.

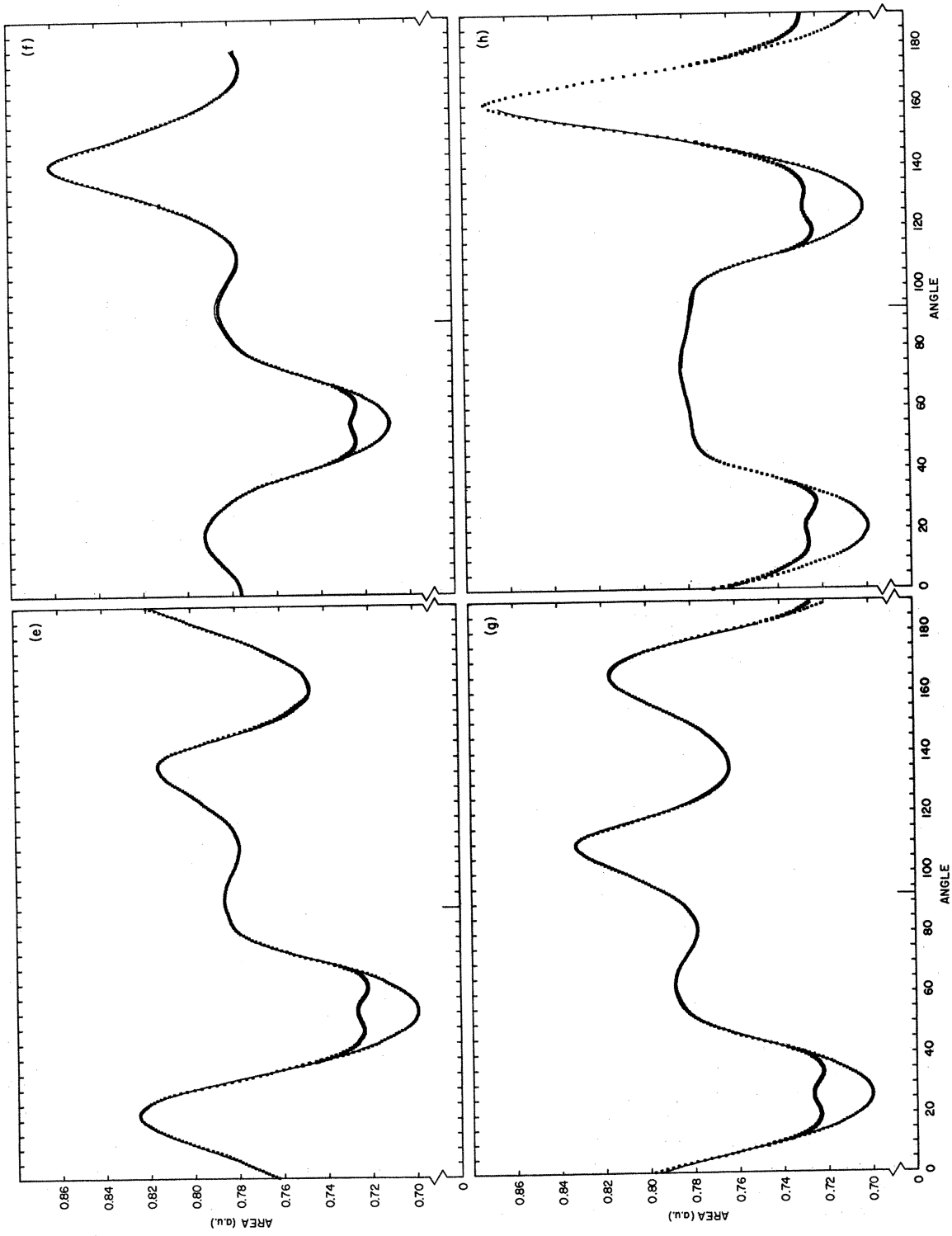

FIG. 7—(*Continued*)

TABLE I. Specification angles for the planes in which dHvA data were taken.

Run	θ_1	φ_1	θ_2	φ_2	α	ψ_0[a]
a	6.74	15.99	90.00	22.23	90.70	100
b	10.01	19.97	90.00	−6.53	90.84	90
c	10.08	20.08	90.00	−39.58	89.25	90
d	22.74	19.06	90.00	224.81	90.02	90
e	22.25	19.48	90.00	237.20	90.07	90
f	22.58	18.96	90.00	248.15	90.66	90
g	23.37	−15.71	90.00	29.43	89.00	92
h	19.30	45.40	90.00	45.40	89.20	92

[a] Value of ψ for field along axis of crystal (i.e., along $\hat{n}_1$ in Fig. 1) for $\alpha = 90.00$. The calibration of the angle monitor does not correspond exactly to rotation in degrees; a change of 10 units in ψ corresponds to a rotation of the sample holder of 10.33°.

Table I lists the specification angles for the eight planes *a*–*h* in which the dHvA effect was studied. We expect runs *d*–*g* to have approximately the same values of θ_1 and φ_1 since these two samples were derived from the same crystal. The fact that they are not exactly the same is understandable since the sample and sample rotator may have a slightly different orientation with respect to the solenoid axis on each run. Also, as mentioned earlier, the rotor of the sample rotator could move in its bearings by as much as $\frac{1}{2}°$ and this can cause a slightly different effective sample axis on each run (which also necessitates the introduction of the cone angle α). The same remarks hold true for runs *a*–*c*.[42]

Figure 6(a) shows a stereographic plot of the eight planes (cones) *a*–*h* studied in this investigation. In Fig. 6(b) we show all the planes *a*–*h*, folded into the basic 1/48th of the unit sphere (appropriate for the Γ-centered surface). Note that there is no point within this basic spherical triangle which is farther than 3° away from a plane in which the magnetic field was rotated. Observe also that the traces do not reproduce themselves in going 180° as discussed in the section on sample orientation theory.

B. Γ-Centered Electron Surface

Figure 7 shows the angular variation of the dHvA frequency for the Γ-centered electron surface when the magnetic field is rotated in "planes" (cones) *a*–*h*. All data in this paper are given in a.u. with momenta measured in reciprocal Bohr radii and energy in Ry. As mentioned earlier, plane *h* is very close to a (110) plane. Note that when the magnetic field is near the [111] direction the surface has two extremal areas. The smaller of these two areas corresponds to the central section of this surface. If the larger area were identified as the central section then there would have to be a third period corresponding to a second maximum area since the topology of this surface demands that any minimum extremal area must be bounded by two maximum extremal areas. The angular variation of the frequency was determined almost entirely from field rotations and thus, as mentioned earlier, the relative accuracy is very high. Data were taken at about 0.35°K to achieve the highest possible amplitude. Near the [110] direction, where the angular dependence of the area is greatest, as many as 80 oscillations per degree were observed. When the amplitude went to zero in the vicinity of a spin splitting zero the number of lost oscillations could usually be determined by extrapolation from the number of oscillations per degree observed on each side of the zero.

We may now take the observed areas in these eight planes and fit them to cubic harmonics. Our criterion for a good fit was the stability of the fit to the area (and the predicted radii) as the number of harmonics was increased above some minimum level ($L=26$ in our case). The radii were observed to be much more sensi-

TABLE II. Area and effective-mass expansion coefficients for the Γ-centered surface.

i	l	β_{il}	γ_{il}	β_{il}'	γ_{il}'
1	0	2.75529	0.87704	8.62899	2.74669
1	4	0.04504	0.03823	0.05819	0.04939
1	6	−0.11231	0.11439	−0.67846	0.69108
1	8	0.01329	0.01547	0.16132	0.18779
1	10	−0.00059	0.00076	0.07192	−0.09302
1	12	0.00895	0.01263	0.09192	0.12970
2	12	−0.01937	−0.02733	−0.16669	−0.23521
1	14	−0.00462	0.00702	−0.07379	0.11213
1	16	0.00024	0.00038	0.00196	0.00318
2	16	0.00142	0.00230	0.05813	0.09422
1	18	−0.00278	0.00478	−0.01535	0.02634
2	18	0.00591	−0.01015	0.06312	−0.10833
1	20	0.00097	0.00175	0.01254	0.02265
2	20	−0.00195	−0.00352	−0.05155	−0.09312
1	22	0.00001	−0.00002	−0.00160	0.00303
2	22	−0.00068	0.00128	−0.03352	0.06345
1	24	0.00044	0.00087	0.00796	0.01572
2	24	−0.00092	−0.00183	−0.00519	−0.01025
3	24	0.00211	0.00418	0.01494	0.02951
1	26	−0.00049	0.00100	−0.02080	0.04272
2	26	0.00085	0.00174	0.02564	−0.05266
1	28	0.00009	0.00020		
2	28	−0.00008	−0.00017		
3	28	−0.00008	−0.00018		
1	30	−0.00008	0.00018		
2	30	0.00025	−0.00055		
3	30	−0.00057	0.00126		

tive than the area. Fits were made with 21, 24, and 27 terms corresponding to $L=26$, 28, and 30. It was observed that the radii at all angles varied by no more than 0.2% between the 21- and 27-term fits. In early attempts where orientations were determined only by the x-ray technique (before the orientation program became operational) it was observed that the radii varied by several percent between the 21- and 27-term fits. This shows that having carfully oriented samples is absolutely essential in order to accomplish the area-to-radii inversion accurately. The higher harmonics are most seriously affected by misorientation. The least-squares fit uses the cubic harmonics, and if the data are misoriented they will not have cubic symmetry with respect to the least-squares fit program. Since the misorientation is on a small angular scale ($\sim 2°$) it will effect only the higher harmonics. Another indication of the quality of our fit is that the coefficients γ_{il} [see Eq. (3b)] are nearly independent of the number of terms used in the fit, above the minimum number $L=26$, as they would be if the coefficients had been projected out of the area function by integration (we are expanding in an orthonormal set). Were the only object of this investigation the determination of Fermi-surface radii we could have obtained a satisfactory fit with less data (we would not have then been able to determine the spin-splitting zero contours, however). When we used only two of the arbitrary planes of oriented data the radii varied by 0.5%, which is to be compared with the 0.2% fit obtained with the eight planes.

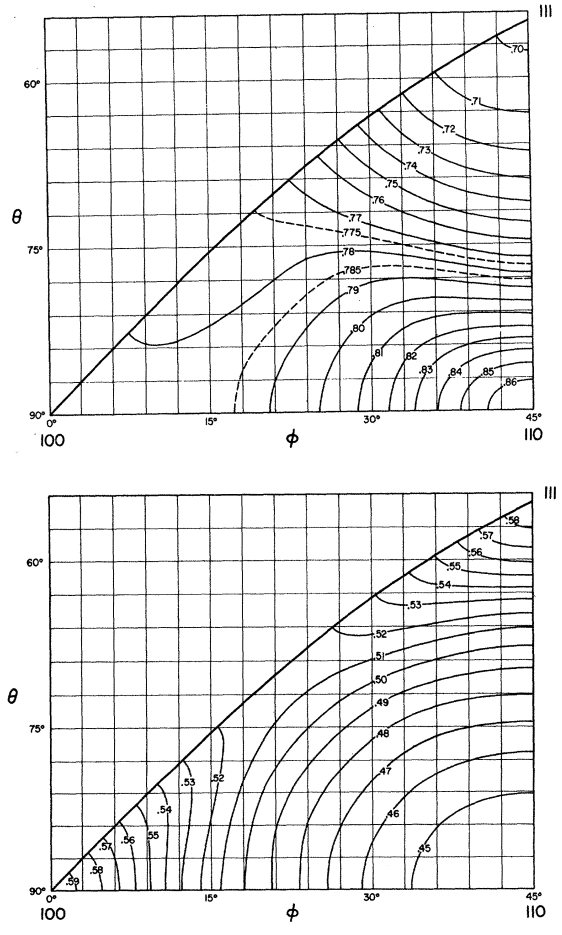

FIG. 8. (a) Contours of constant area for the Γ-centered surface in the basic triangle. (b) Contours of constant radius for the Γ-centered surface in the basic triangle.

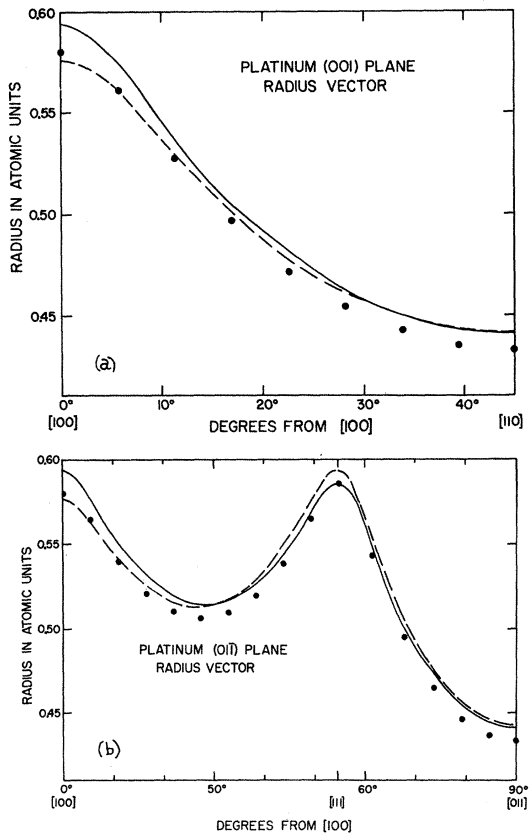

FIG. 9. (a) Solid line shows the radius of the Γ-centered electron surface in the (100) plane. The filled dots are the calculations of Andersen and Mackintosh, while the dashed line is the calculation of Mueller, Ketterson, Windmiller, and Hörnfeldt. (b) Solid line shows the radius of the Γ-centered electron surface in the (110) plane. The filled dots are the calculations of Andersen and Mackintosh, while the dashed line is the calculation of Mueller, Ketterson, Windmiller, and Hörnfeldt.

Table II contains the coefficients γ_{il} and β_{il} of Eq. (3) for the 27-term fit ($L=30$). The solid lines in Fig. 7 were calculated from the fit. We observe that a rather good fit is achieved for all the data. The period normalization correction (A_0) has been included in the experimental data. Figure 8(a) shows a topographic map of the area (contours of constant area) in the basic triangle.

The accuracy achieved in fitting the area gives us confidence that the deduced radii are also quite accurate. Figures 9(a) and 9(b) show the Fermi radius in the (100) and (110) planes. Shown also are the radii from the band-structure calculations of Andersen and

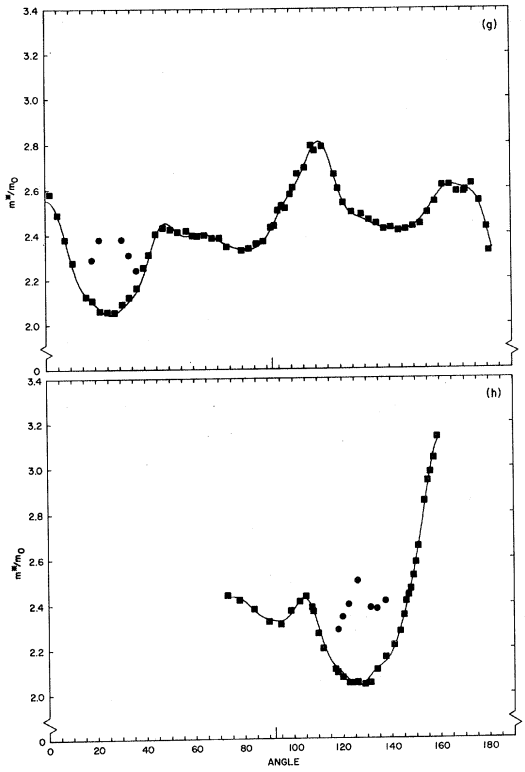

FIG. 10. Observed cyclotron effective masses for the Γ-centered surface for runs g and h. The solid lines show the $L=26$ fit to the data. The angular scale corresponds to the experimental coordinate ψ as shown in Fig. 6.

Mackintosh[4] together with those of Mueller, Ketterson, Windmiller, and Hörnfeldt.[5] Figure 8(b) shows the contours of constant radius in the basic triangle. From the deduced radii we calculated the volume of this surface using Eq. (6a). We find $4.19\times10^{-3}a_0^{-3}$ or 0.426 electrons/atom.

After the completion of run f, the Texas Instruments precision pressure gauge was acquired and this allowed accurate temperature measurements to be performed. In addition, great care was taken to ensure that the amplifier-detection system was highly linear and that gain of neither the oscillator-power amplifier or amplifier-detection system changed with time. As a result of these precautions, measurements of the cyclotron mass (by observing the temperature dependence of the dHvA amplitude) with an accuracy of about $\frac{1}{2}\%$ were possible. This is about the same accuracy as can be achieved using the cyclotron resonance technique. The dHvA method of determining effective masses has several advantages, however. All of the dHvA period discrimination techniques may be employed; also the requirements on sample purity are not as severe since the dHvA measurements are carried out at higher magnetic fields. Furthermore the preparation of the strain-free polished surfaces necessary in doing cyclotron resonance work is quite difficult. Lastly, the phase of the cyclotron resonance oscillations is usually quite low and this results in lower accuracy due to the limited number of observed resonances. A word of caution is in order at this point. When measuring very light masses or when performing measurements at very low temperature, an exponential approximation to the sinh term in Eq. (1) is not valid. Furthermore, BH effects[43,44] also cause deviations from expression (1) in this limit. The masses of the carriers observed and the temperatures used in this experiment were such that no corrections of these kinds were needed.

Figure 10 shows the observed cyclotron effective masses for the Γ-centered surface for runs g and h, respectively. As remarked earlier, run h is very nearly a (110) plane. Note that the general anisotropy of the cyclotron effective mass in the (110) plane is very similar to the area, there being however an extra "bump" between the [100] and [111] directions. The effective masses of the two frequencies observed near [111] have been deduced by observing the amplitude of the oscillations at the beat maxima and also at the beat waist, and then solving for the separate amplitudes. The observed masses are quite high compared with those usually observed in nontransition metals.

In order to interpolate the observed effective masses to other angles (needed for deducing g factors from spin-splitting zeros) and furthermore to determine the Fermi velocity using Eq. (5), we have least-squares fitted the observed cyclotron masses to the cubic harmonic expansion given in Eq. (4). The coefficients β_{il}' resulting from this fit are given in Table II. A 21-term fit (corresponding to $L=26$) was used. It is observed that the higher l values in the cyclotron mass fit fall off less rapidly than do the coefficients of the area fit. Part of this is due to the fact that the anisotropy of the cyclotron mass is greater than the area. More of it is probably caused by the lower inherent accuracy of the cyclotron mass data. For this reason we report only a

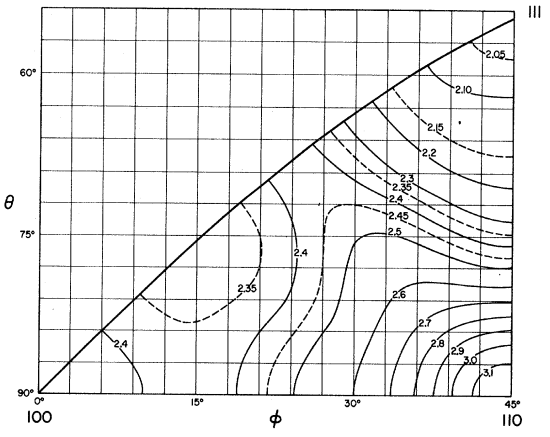

FIG. 11. Contours of constant effective mass for the Γ-centered surface resulting from the $L=26$ fit to the data.

21-term fit since the higher coefficients are probably not significant, although fits using 24 and 27 terms were also attempted. The interpolated masses varied by only a few tenths of a percent between these three fits, but the Fermi velocities (to be discussed shortly) varied by about 5%. The solid lines in Fig. 10 show the 21-term fit to the effective masses for these two planes. It will be observed that the over-all fit achieved is rather good. Figure 11 shows a contour map of the interpolated cyclotron effective mass in the basic triangle using the 21-term fit.

Having the coefficients γ_{il} and γ_{il}' we can calculate the three components of the Fermi velocity for the Γ-centered surface using Eqs. (5a)–(5c). Figures 12(a) and 12(b) show the components v_p and v_θ in the (100) and (110) plane, respectively. Shown also are the calculations of Andersen and Mackintosh[4] together with those of Mueller, Ketterson, Windmiller and Hörnfeldt.[5] Note that v_φ is zero by symmetry in these two planes. The angular dependence is not as smooth as one would like, but the magnitude and anisotropy are

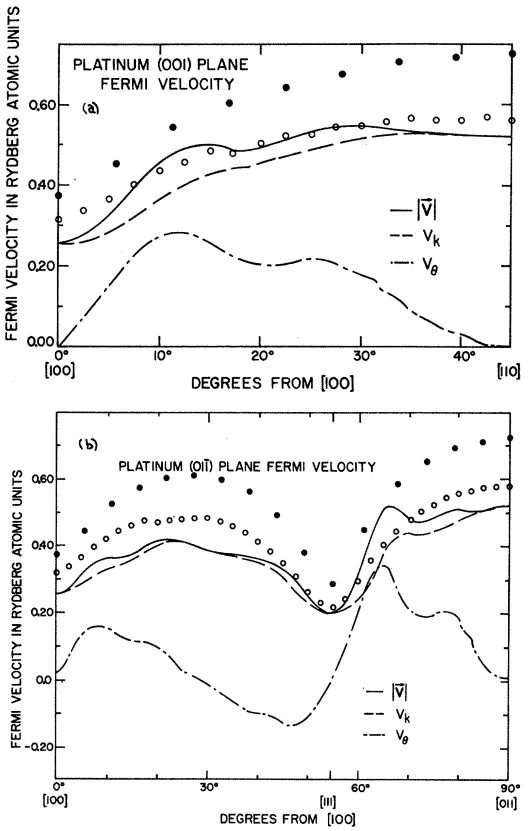

FIG. 12. (a) v_p and v_θ for the Γ-centered surface in the (100) plane. v_φ is zero by symmetry. The filled circles show v_p as calculated by Andersen and Mackintosh, while the open circles show v_p as calculated by Mueller, Ketterson, Windmiller, and Hörnfeldt. (b) v_p and v_θ for the Γ-centered surface in the (110) plane. v_φ is zero by symmetry. The filled circles show v_p as calculated by Andersen and Mackintosh, while the open circles show v_p as calculated by Mueller, Ketterson, Windmiller, and Hörnfeldt.

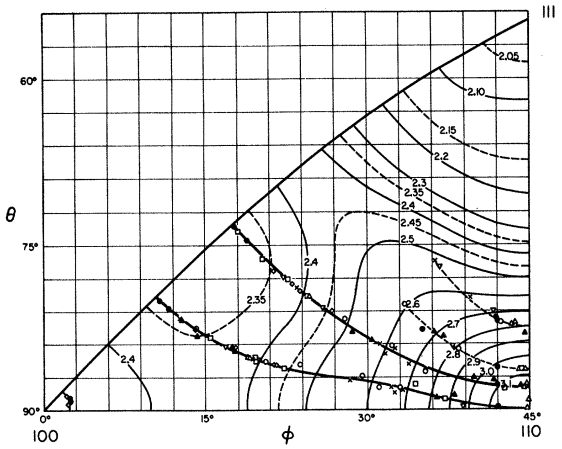

FIG. 13. Angles at which spin-splitting zeros were observed for the Γ-centered surface. Shown also are the contours of constant effective mass.

determined satisfactorily. The small oscillations result from the lower inherent accuracy of the cyclotron mass data, and, were more cyclotron mass data taken in other planes, the accuracy could be improved. As already remarked, the predicted velocities varied by about 5% for 21-, 24-, and 27-term expansions in Eq. (4), and we thus set 5% as the accuracy of our determination of the Fermi velocity. In determining the $\hat{\theta}$ and $\hat{\varphi}$ components of the velocity it will be observed that the angular derivatives of the radius enter, and thus any small spurious oscillations in the radius fit become amplified. This is not felt to be important here, however, owing to the very superior stability of the predicted radii as the number of terms in the expansion was increased.

We may now use the calculated radii and velocities to compute the density of states for the Γ-centered surface from Eq. (7). By numerical integration we obtain $N(E_F)=6.24\times10^{-2}a_0^{-3}\,\mathrm{Ry}^{-1}$ or 6.35 electrons/atom Ry.

Once the cyclotron mass has been determined we may deduce the Dingle-Robinson temperature by observing the magnetic field dependence of the dHvA amplitude. This was done at several angles and generally T_x was in the range 0.3–0.5°K.

The dHvA amplitude was observed to disappear, independent of the magnitude of the applied magnetic field, for many field directions ψ in each of the runs *a–h*. (Angles at which the amplitude vanished owing to the sample magnetization being perpendicular to the pickup coil were calculated and are not considered here.) These have been identified as spin-splitting zeros caused by the term $\cos(\frac{1}{4}g\partial A/\partial E)$ in Eq. (1b) vanishing. This occurs when $\frac{1}{4}g(\theta,\varphi)[\partial A(\theta,\varphi)/\partial E]=(2r+1)\frac{1}{2}\pi$ or equivalently when $m^*(\theta,\varphi)/m_s(\theta,\varphi)=r+\frac{1}{2}$ where r is an unknown integer. Physically the dHvA amplitude disappears because the energy spacing between two adjacent Landau levels is exactly one-half the spacing

TABLE III. Comparison of experimental results with RAPW band calculation of Andersen and Mackintosh (Refs. 4 and 24).

	Extremal areas a.u.		Cyclotron masses m^*/m_0			Fermi momentum a.u.	Fermi velocity a.u.	g Factor
	Expt	Theory	Expt	Theory	Ratio	Expt	Expt	Expt
Γ-centered electrons								
[100]	0.778	0.751	2.44	1.69	1.44	0.594	0.255	2.06
[111]	0.695	0.676	2.06	1.42	1.54	0.585	0.195	•••
[110]	0.865	0.842	3.16	2.05	1.45	0.440	0.518	1.59
X-centered holes (principal ellipsoid)								
[100]	0.00298		0.272[a]			0.0483	0.145	
[111]			0.363	0.30	1.21			
[110]	0.00467		0.426[b]			0.0308	0.227	
Open-hole surface								
[100] α orbit	0.0744	0.0713	1.53	0.91	1.68			
[110] β orbit		0.341		6.23	•••			
[110] γ orbit	0.218	0.217	3.28	1.93	1.70			
[110] δ orbit	0.182	0.172	3.62	2.78	1.30			

[a] Calculated from the [110] mass (see footnote below) and the [100] and [110] principal areas.

[b] Determined from nonprincipal [100] mass assuming an ellipsoid-of-revolution model.

between the levels in the absence of electron spin and thus the first harmonic of the dHvA frequency must disappear. In Fig. 13 we have plotted, in the basic triangle, all the angles at which spin-splitting zeros were observed for the Γ-centered surface. These points fall quite nicely on five separate contours three of which are shown by heavy solid lines (note the one very close to [100]) and two by dashed lines. Geometrically the spin-splitting zero contours may be thought of as the intersection of two surfaces with a common center, one with "radius" $m^*(\theta, \varphi)$, and the other with "radius" $(r+\frac{1}{2})m_s(\theta, \varphi)$. The locus of *intersection* of two such surfaces must be a closed curve. Note that the two dashed curves appear to end abruptly near the center of the basic triangle. This can happen only if the surfaces are *tangent* over the length of the dashed contours and then separate. Since true tangency would be an unlikely accident we interpret this to mean only that the surfaces are extremely close to each other on these two contours. The possibility that the two dashed contours join does not appear to be supported by the data. However, it will be useful to follow this point in some future investigation. Shown for reference in Fig. 13 are the contours of constant effective mass. Were the g factor equal to its free-space value of 2 then the spin-splitting zero contours would have been identical to the 2.5 m_0 effective-mass contour (where $r=2$ in this case). The spin-splitting zero contours and the $2.5m_0$ effective-mass contour are, however, quite different. Indeed one spin-splitting contour cuts across the effective-mass contours from the region of maximum to minimum mass. Clearly the g factor is different from 2 and anisotropic. We have taken the data of Fig. 13 and fit it to cubic harmonics on the assumption of a value of $r=2$. Such a procedure is justified only if we assume that the spin mass is more smoothly varying than the cyclotron mass. We choose the value $r=2$ since it is the only one that would intersect the effective-mass surface in the absence of spin-orbit coupling and many-body effects ($g=2$), and we thus assume these effects do not greatly alter the g factor. It was observed that the (100) plane spin-mass fit converged after the first few terms thus justifying our fitting procedure. Figure 14 shows the spin mass in the (100) plane using a 9-term fit. An extrapolation into the (110) plane would not be reliable since no spin-splitting zeros were observed in the vicinity of [111].

We have collected the areas, radii, cyclotron masses, velocities, and g factors for the [100], [111], and [110] directions in Table III. Shown for comparison are the corresponding quantities as calculated by Andersen and Mackintosh[4] using the RAPW technique.

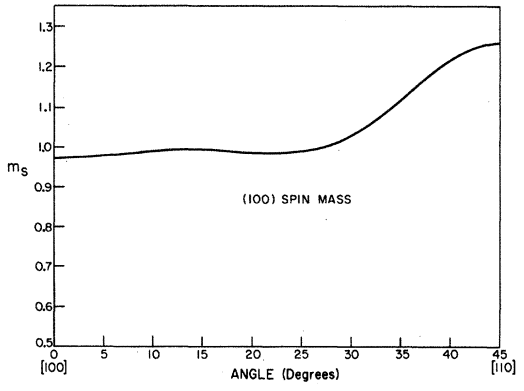

FIG. 14. (100) plane spin mass m_s resulting from a nine-term fit to the data in Fig. 13.

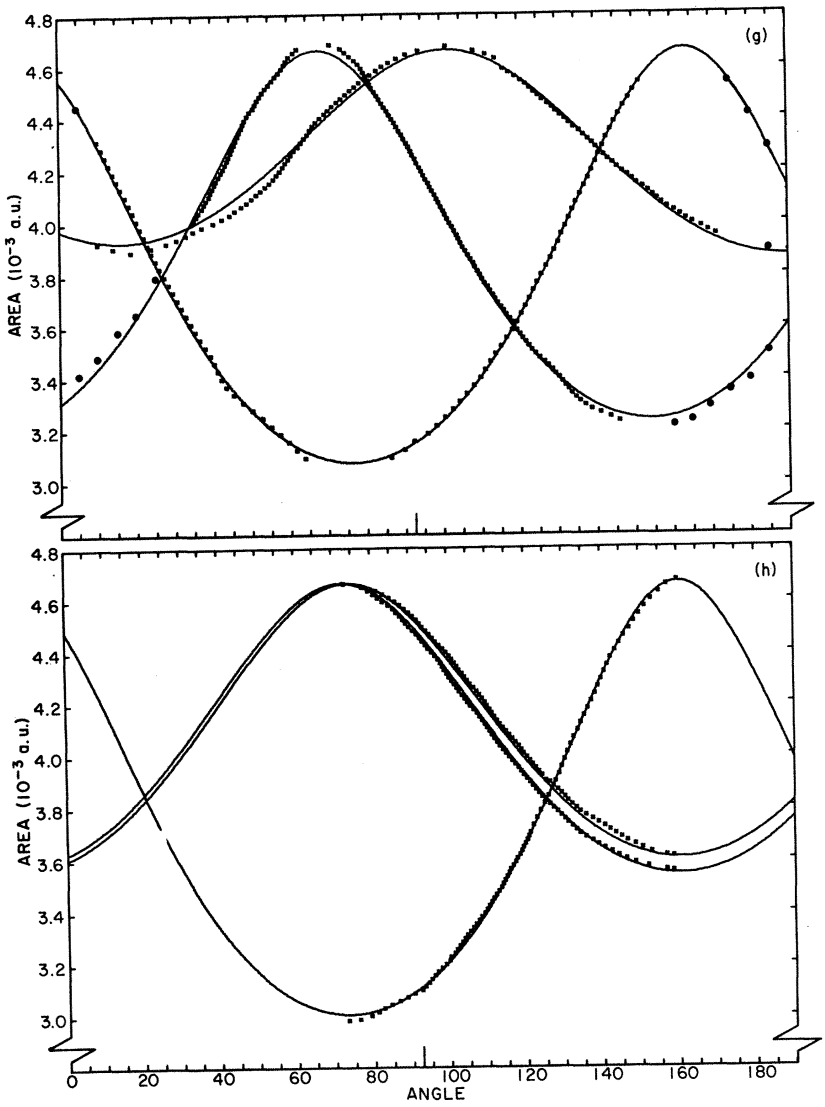

FIG. 15. Observed areas of the X-centered hole pocket for runs g and h. The solid lines show an $l=2$ fit using the spherical mapping techniques. The angular scale corresponds to the experimental coordinate ψ as shown in Fig. 6.

C. X-Centered Hole Pocket

Figure 15 shows the observed areas of the X-centered hole pocket in runs g and h. Were we rotating exactly in a (110) plane the two nearly coincident branches in run h would have been degenerate, and these branches correspond to the nonprincipal ellipsoids. For the principal ellipsoid, and with the magnetic field along [100], we measure the cross section in the XWU plane and for the nonprincipal ellipsoid, we measure the cross section in the $XW\Gamma$ plane. For the magnetic field along [110], we measure the cross section of the principal ellipsoid in the $XU\Gamma$ plane. Note that we have very nearly a surface of revolution since the $XW\Gamma$ cross section is almost identical to the $XU\Gamma$ (upper branch at [100] and [110], respectively, in Fig. 15 run h). For an arbitrary magnetic field direction there will be three frequencies. All three branches of this carrier were observed at nearly all values of ψ in runs a–h. Since the data follow so well an ellipsoidal model we have reported only planes g and h. Note that all three branches are clearly resolved. The solid lines in Fig. 15 result from a fit using the spherical mapping procedure. The fit included the $l=0$ and $l=2$ terms only and thus corresponds to an ellipsoidal fit.

Alternatively, one could fit the data to an expression of the form

$$[A^2(\theta,\varphi)]^{-1}=\sum_{lm}\alpha_{lm}C_{lm}(\theta,\varphi). \qquad (13)$$

For an ellipsoid (or any second-order surface) this expression terminates with the $l=2$ terms. If we choose the z axis as the fourfold axis then the only nonvanishing terms will be α_{00} and α_{20}.

The spherical mapping procedure has the advantage that all areas in the transformed system are approximately the same and thus receive equal weighting in the least-squares fit. Were we to choose the optimal value

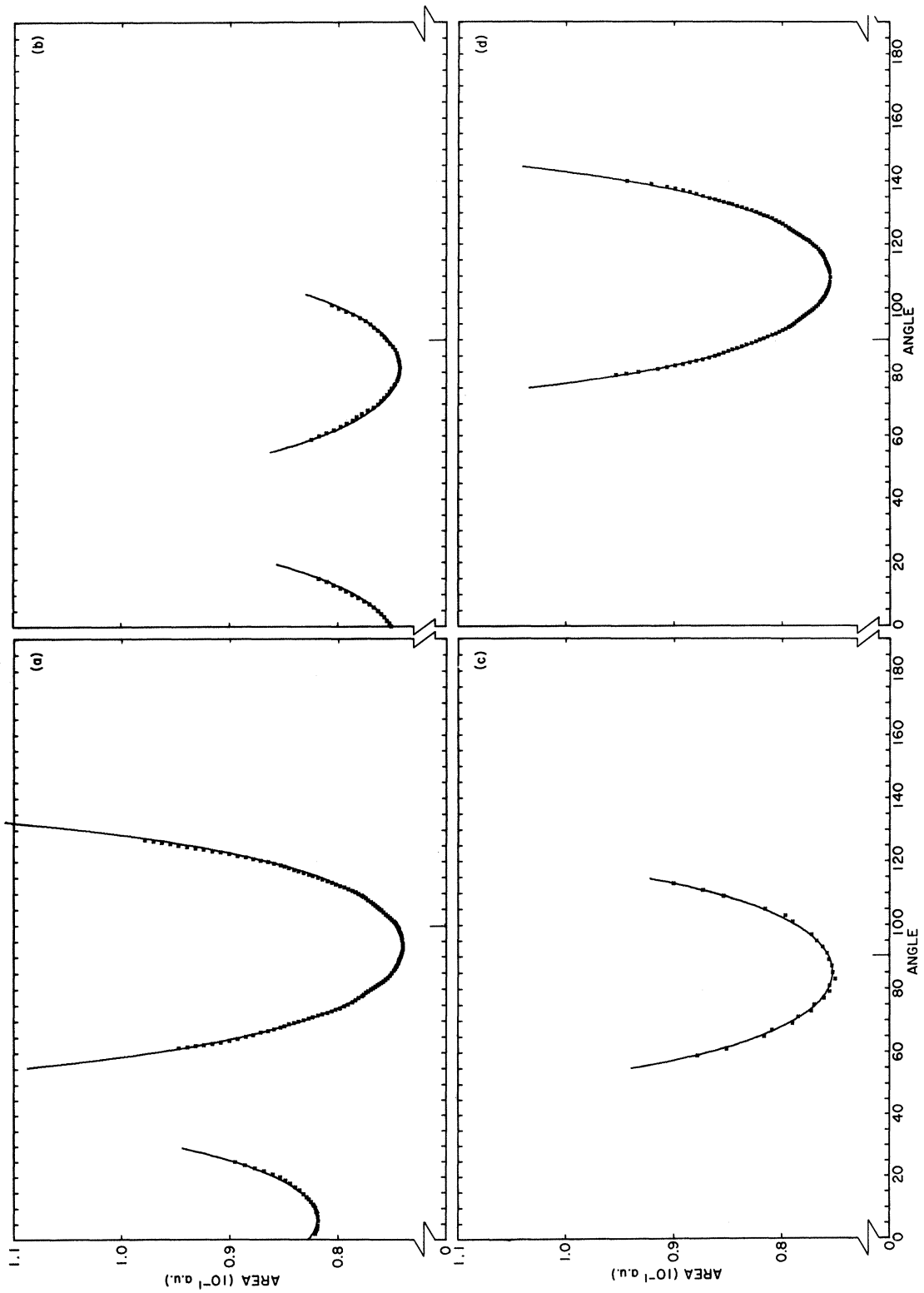

FIG. 16. Extremal areas corresponding to the α orbit observed in runs a–h. The solid lines show a fit to Eq. (13). The angular scale corresponds to the experimental coordinate ψ as shown in Fig. 6.

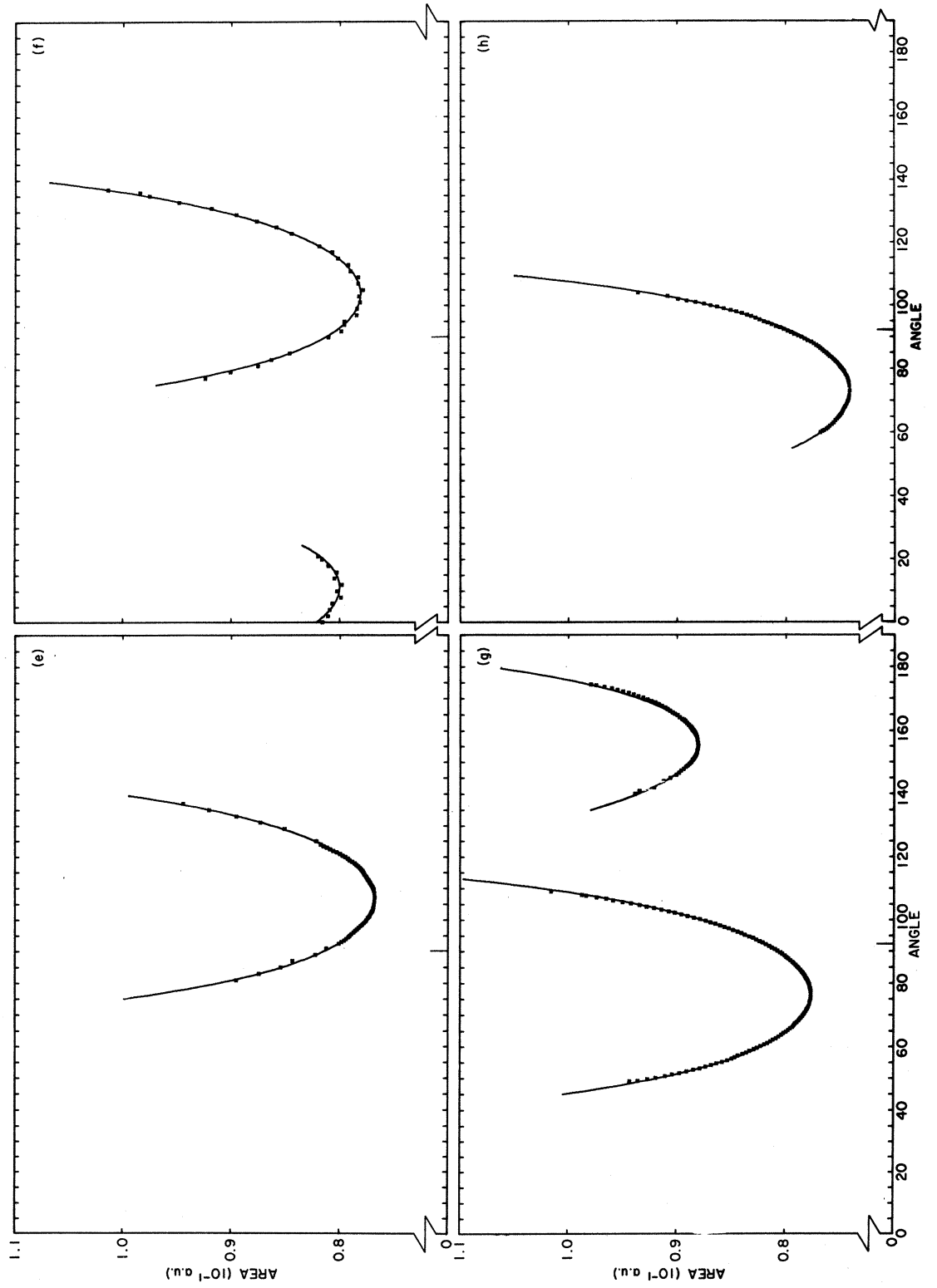

FIG. 16.—(*Continued*)

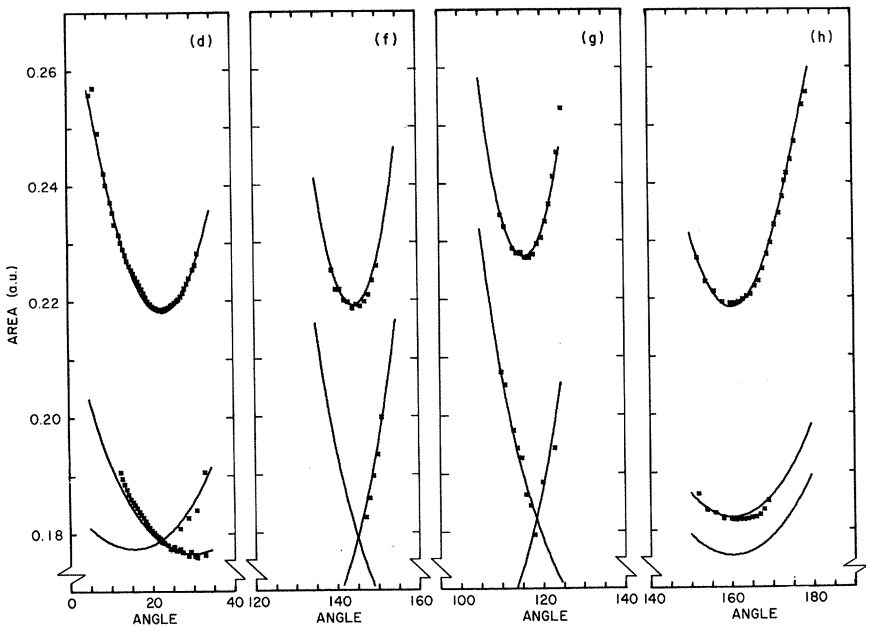

FIG. 17. Extremal areas corresponding to the γ and δ orbits observed in runs *d*, *f*, *g*, and *h*. The solid lines are a fit to Eq. (13). The angular scale corresponds to the experimental coordinate ψ as shown in Fig. 6.

of the transformation parameter γ then the $l=2$ term would vanish since the data for an ellipsoid would be mapped into a sphere. In practice what is done is to select an approximate value for γ and then the $l=2$ term in the fit will account for the small residual deviations from a sphere in the transformed system. The data for the two nonprincipal ellipsoids are also included in the fit. This is accomplished by performing 90° rotations about the appropriate [100] axis such that all ellipsoids have the z axis as the fourfold axis. The values of γ and the expansion coefficients in the transformed system β_{lm} are

$$\gamma=0.641, \quad \beta_{00}=1.0622\times10^{-2}, \quad \beta_{20}=0.0017\times10^{-2}.$$

Fits were also extended through the $l=6$ terms. While some deviation of the predicted radii from ellipticity was observed, it was not considered to be statistically significant and thus radii deduced from these fits will not be reported. The principal areas and radii resulting from the fit for $l=2$ are given in Table III.

Three effective masses were measured for these carriers. The nonprincipal [100] mass, the [111] mass, and the nonprincipal [110] for which we observed 0.426, 0.363, and 0.327, respectively. We may use the nonprincipal [100] mass (which is the same as the principal [110] mass $m_\perp{}^*$ for an ellipsoidal model), the two principal areas $A_\perp$ and $A_{||}$, and an ellipsoidal parabolic model to determine all the relevant parameters for this surface. The areas, radii, and velocities of the principal ellipsoid in the [100], [111], and [110] directions are given in Table III. For the number of carriers per ellipsoid we find $n(E_F)=1.546\times10^{-6}a_0^{-3}$ or 1.57×10^{-4} holes/atom. For the density of states per ellipsoid we find $N(E_F)=6.647\times10^{-4}a_0^{-3}$ Ry^{-1} or 6.75×10^{-2} holes/atom Ry.

D. Open-Hole Surface

Figures 5(b) and 5(c) show the open-hole surface in Pt. The topology of this surface [as seen in Fig. 5(b)] is that of cylinders, extending in the [100] directions and intersecting in pairs at the points X of the Brillouin zone. For the magnetic field along the [100] axis two extremal sections are expected. One section, the ϵ orbit in Fig. 5(c), runs around the inside of the lattice formed by the intersecting "cylinders." The unenhanced cyclotron effective mass of this orbit is calculated[20] to be 4.95 corresponding to an enhanced mass of order 7. Such a large mass was not observable in the present experiment. The other expected orbit, the α orbit, runs around one of the "cylinders" and is centered (for the field along [100]) on the point W. This orbit has a rather small effective cyclotron mass (the smallest observed on the open-hole surface) and was observed over a wide range of magnetic field directions about [100]. For the field along [110], both the calculations of Mueller, Ketterson, Windmiller and Hörnfeldt[5] and those of Andersen and Mackintosh[4] predict three extremal cross sectional areas, the β, γ, δ orbits in Fig. 5(c). The β orbit, around a junction of two of the "cylinders" and centered on the point X, is an area maximum. However, the RAPW calculations[4] predict an unenhanced cyclotron effective mass for the β orbit of 6.23 (while Ketterson, Mueller and Windmiller[20] find 5.79), too heavy to be observed in this experiment. The area minimum within the junction corresponds to the noncentral γ orbit while the δ orbit corresponds to an orbit outside the junction about a "cylinder." Both the γ and δ orbits were observed in the present experiment. Note that as the field is turned away from [110] in a plane different from (110) the area branch corresponding to the δ

orbit splits into two branches corresponding to the two unlike orbits about the [100] and [010] "cylinders." The area branch corresponding to the γ orbit must remain single valued, and this fact was used to distinguish the various branches. The angular dependence of the area and effective mass for the various orbits on this surface have been calculated by Ketterson, Mueller, and Windmiller[20] using the Fourier-series approach and the band structure of Mueller, Ketterson, Windmiller, and Hörnfeldt.[5]

Figure 16 shows the experimentally observed areas of the α orbit in runs a–h while Fig. 17 shows the γ and δ orbit areas observed in runs d, f, g, and h. The angular dependence of the α-orbit area was found to be hyperbolic (rather than parabolic as expected for a cylinder). The disappearance of this frequency near 30° is quite abrupt and thus probably results from geometrical causes, i.e., the orbit ceases to exist.

Figure 17 run h shows the γ and δ orbits near [110] in an approximate (110) plane. The lower branch splits into two subbranches when the magnetic field is tipped out of the (110) plane and thus arises from the δ orbit. The upper branch near [110] is identified as the γ orbit. The angular dependence of both the γ and δ frequencies is also hyperbolic rather than parabolic. In the Fourier-series calculations[20] the center of the δ orbit was considerably removed from the point W. This fact complicated calculations on the δ orbit and, in particular, it was not determined if the α and δ orbits are, in fact, the same orbit. Experimentally they appear to be geometrically distinct.

The smooth curves through the α-, γ-, and δ-orbit data points were generated by fitting each of the data sets to a separate expression of the form given in Eq. (13). For second-order surfaces such as an ellipsoid, cylinder, or hyperboloid, the expression terminates after the $l=2$ terms. The allowed values of l and m in Eq. (13) depend on the symmetry of the data. Since the extremal area is invariant under the transformation $\hat{H}\rightarrow-\hat{H}$, only even l occurs in the summation [the parity for spherical harmonics being $(-1)^l$]. The appropriate harmonics for the ϵ orbit would be Kubic harmonics since the orbit is centered on the point Γ which has full cubic symmetry. Similarly we would use the harmonics associated with the point group of X for the β orbit. The point X has the symmetry D_{4h}. If we choose the X-Γ line as the z axis then we have $m=0$ (mod 4). As stated earlier however, neither of these orbits was observed in this experiment.

TABLE IV. Expansion coefficients α_{lm} of Eq. (13).

	α orbit area	α orbit mass	γ orbit	δ orbit
α_{00}	14.171	−1.2865	77.618	54.247
α_{20}	307.298	1.4909	105.355	68.126
α_{40}	−18.627	−0.1803	42.627	−13.097
α_{44}	42.083	0.4906	−30.088	4.653

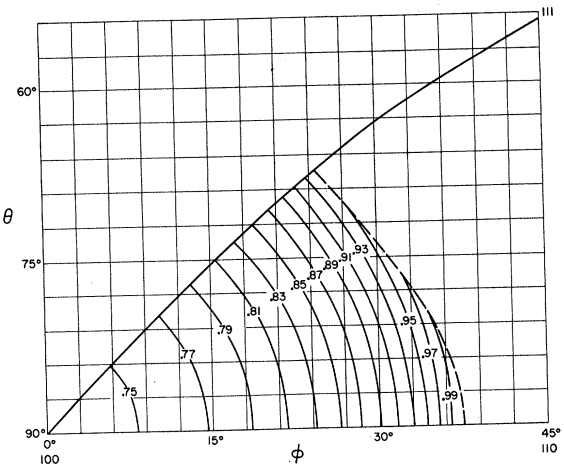

FIG. 18. The solid lines are the contours of constant area for the α orbit. The dashed line shows the boundary on which the orbit ceases to exist.

We next consider the α orbit. The angular dependence of the α orbit is governed by the symmetry of the point W. The point-group symmetry of W is D_{2d}. This group contains eight elements. The X-W line is chosen as the principal axis and is invariant under the operations C_2 (twofold rotations) and $2S_4$ (fourfold rotation followed by inversions or equivalently fourfold rotation followed by reflection through a plane containing the point W and perpendicular to X-W). The crystal is invariant to twofold (U_2) rotations about each of the two mutually perpendicular W-L axes. The two planes σ_d of reflection symmetry are the ΓXW and WXU planes. With the identity operator this completes the enumeration of the eight elements.

If the magnetic field lies along a [100] axis (along the X-W line) there must be an extremal orbit which includes the point W. Consider the area as a function of displacement along the X-W line. Because of the rotary-reflection symmetry of W, for each orbit measured along X-W, there is a corresponding orbit, on the other side of W, with equal area which is however rotated 90° about X-W. Thus an extremum must exist at W. Furthermore this extremal orbit will have square symmetry since the rotary-reflection symmetry degenerates to fourfold symmetry for the plane perpendicular to the X-W line which includes W. The orientation of the "square" is such that the reflection through σ_d is satisfied. As the magnetic field is tipped away from X-W in a general direction the extremal orbit need not include the point W and the orbit will in general have no symmetry. The observed extremal area will, however, show fourfold symmetry with respect to rotations of $\hat{H}$ about the X-W axis. Again this follows from the fourfold rotary-inversion symmetry of the point W. For each point on an extremal orbit there is an identical point on another extremal orbit which is rotated 90° about X-W and inverted through W. Thus the measured

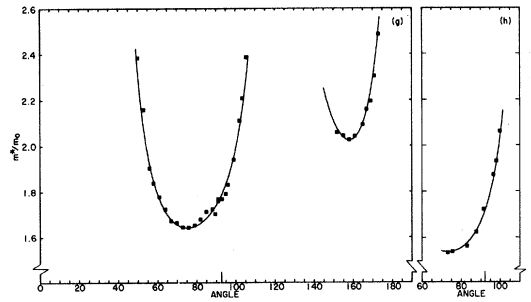

FIG. 19. The angular dependence of the effective masses of the α orbit observed in runs g and h. The angular scale corresponds to the experimental coordinate ψ as shown in Fig. 6.

area shows the higher point-group symmetry D_{4h}. Incidentally, if the magnetic field is tipped away from X-W in a (110) plane, the plane of the orbit will always contain the point W. We have already shown that for the field along (100) the extremal orbit is centered at W. As the magnetic field is rotated from W-X to W-L [i.e., in a (110) plane] the orbits will cut the W-L axis. For each orbit which cuts the W-L axis on one side of W there is an identical orbit, rotated 180° about $\hat{H}$ and reflected through the (110) plane, which cuts an equal distance on the other side of W. This follows from the fact that the second mutually perpendicular W-L axis is a twofold axis (U_2). Thus the orbit containing W must be extremal.

The symmetry of the observed extremal area of the δ orbit is the same as that of the α orbit, i.e., we expand in D_{4h} harmonics.

For the magnetic field in the vicinity of [110] the γ orbit does not include the point X. Actually there are

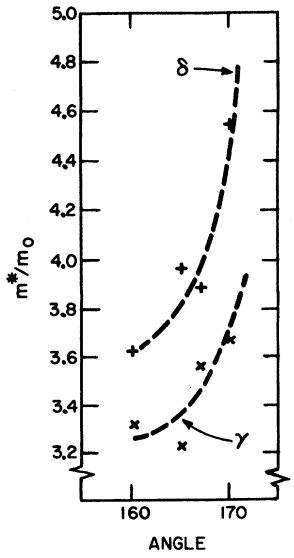

FIG. 20. The angular dependence of the effective masses of the γ (lower) and δ (upper) orbits observed in run h. The angular scale corresponds to the experimental coordinate ψ as shown in Fig. 6.

two γ orbits whose areas are degenerate due to the inversion symmetry of the point X. As the field is tipped away from (110) the distance between the planes of the γ and β orbits decreases[20] and the two may ultimately merge providing the orbits do not cease to exist due to the geometrical features of the open surface. The appropriate harmonics to expand the observed extremal area of the γ orbit are the D_{4h} harmonics with the Γ-X direction as the z axis.

The coefficients α_{lm} used to fit the observed areas for the α, γ, and δ orbits are given in Table IV. Having an analytic expression for the areas we can generate contours of constant area. We do this only for the α orbit since this is the one orbit on the open surface which was observed over a wide range of angles. Figure 18 shows

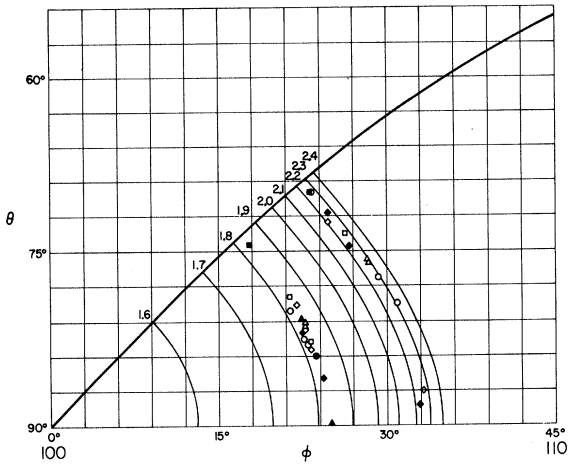

FIG. 21. Angles at which the dHvA amplitude vanishes (owing to spin splitting) for the α orbit. Shown also are the contours of constant effective mass.

such a contour map. The solid lines show the contours of constant area, while the dashed line shows the boundary outside of which the orbit was not observed for geometrical reasons.

The angular dependence of the effective mass for the α, γ, and δ orbits was studied in runs g and h. Figure 19 shows the data for the α orbit while Fig. 20 shows the same thing for the γ and δ orbits. The smooth curves are generated by fitting the data to Eq. (13) in the identical manner used to fit the area data. Table IV also lists the coefficients used to fit the effective-mass data for the α orbit. Figure 21 shows the contours of constant cyclotron effective mass data for the α orbit which were generated from the fit. Included also in Fig. 21 are the angles in runs a–h at which spin-splitting zeros were observed. Here we have a case slightly different from that for the Γ-centered surface. While the spin-splitting zeros do not lie on a contour $(r+\frac{1}{2})m_0$, they do fall on effective-mass contours. Thus the g factor is anisotropic and different from 2, but contours of

constant g run parallel to the contours of constant effective cyclotron mass.

Figure 22 shows the angles at which spin-splitting zeros were observed for the δ orbit near [110]. The contours of constant effective mass are not known as precisely for this orbit, owing to its heavy mass and consequent low amplitude, as for the other orbits considered here. It appears, however, that the contour closest to [110] runs near the 3.5 effective cyclotron mass contour (indicating a g factor near 2) but the other spin-splitting zeros can only be explained by a g factor differing from 2 by about 20%.

We have collected the extremal areas and effective masses for the α, γ, and δ orbits along symmetry planes in Table III. Also listed are the theoretical values.[4] It will be observed that the agreement between the calculated and measured values is quite good.

Our values for the density of states of the Γ-centered surface and X-centered pocket may be combined with the measured heat capacity density of states to determine the density of states of the open surface. Using the value $N(E_F)=37.90$ states/atom Ry for the total electronic density of states derived from the heat-capacity measurements of Dixon, Hoare, Holden and Moody[45] together with our calculated values for the Γ-centered surface and the three X-centered pockets we find $N(E_F)=31.35$ holes/atom Ry for the open surface. By invoking charge neutrality we can calculate the number of carriers in the open surface for which we find $n(E_F)=0.426$ holes/atom.

VIII. CONCLUSIONS

As the reader will observe, the amount of data collected here is rather extensive. The agreement obtained between the experimental Fermi surface and the first-principles calculations of AM is really quite good. Nonetheless an effort should be made to improve the accuracy of the calculations either using first-principles theories or parametrization techniques. The effective mass and its Fermi-velocity inversion are another story.

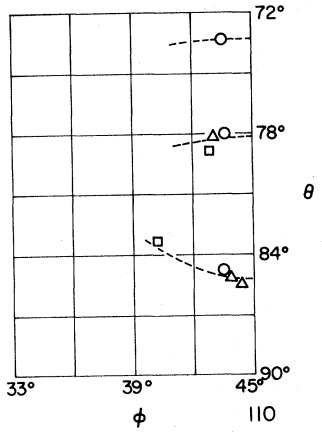

FIG. 22. Angles near [110] of the observed spin-splitting zeros for the γ orbit. The dotted lines indicate the general direction of the spin-splitting contours.

It is hoped that these latter data will inspire a frontal attack on the calculation of electron-phonon and paramagnon mass enhancement.[46,47] As these experiments show, the accuracy of the band structures must be improved along with the application of the many-body theory. Lastly, the g-factor data appear to lie outside the capability of present theory and call for a reexamination of the theory of the g factor both from a single-particle and many-particle point of view.

ACKNOWLEDGMENTS

We would like to thank James Tait for assembling much of the equipment and also for preparing some of the single crystal samples used. Bill Rosevear and Sven Hörnfeldt assisted in taking a portion of the data. We enjoyed many useful theoretical discussions with F. M. Mueller on several aspects of this work. We would like to thank O. K. Andersen and A. R. Mackintosh for communicating their results to us and allowing us to quote these results in our earlier publications.

* Work performed under the auspices of the U.S. Atomic Energy Commission.

[1] J. Rayne, Phys. Rev. **95,** 1428 (1954).
[2] D. W. Budworth, F. E. Hoare, and J. Preston, Proc. Roy. Soc. (London) **A257,** 250 (1960).
[3] S. Foner, R. Doclo, and E. J. McNiff, Jr., J. Appl. Phys. **39,** 551 (1968).
[4] O. K. Andersen and A. R. Mackintosh, Solid State Commun. **6,** 285 (1968).
[5] F. M. Mueller, J. B. Ketterson, L. R. Windmiller, and S. Hörnfeldt (unpublished).
[6] A. B. Migdal, Zh. Eksperim. i Teor. Fiz. **34,** 1438 (1958) [Soviet Phys. JETP **7,** 996 (1958)].
[7] L. D. Landau, Zh. Eksperim. i Teor. Fiz. **30,** 1058 (1956) [Soviet Phys. JETP **3,** 920 (1956)].
[8] L. Onsager, Phil. Mag. **43,** 1006 (1952).
[9] I. M. Lifshitz and A. M. Kosevich, Zh. Eksperim. i Teor. Fiz. **29,** 730 (1955) [Soviet Phys. JETP **2,** 636 (1956)].
[10] I. M. Lifshitz and A. V. Pogorelov, Dokl. Akad. Nauk. SSSR **96,** 1143 (1954).
[11] F. M. Mueller, Phys. Rev. **148,** 636 (1966).
[12] L. L. Foldy, Phys. Rev. **170,** 670 (1968).
[13] F. M. Mueller and M. G. Priestley, Phys. Rev. **148,** 638 (1966).
[14] R. Aurbach, J. B. Ketterson, F. M. Mueller, and L. R. Windmiller, ANL Report No. ANL 7659 (unpublished).
[15] J. B. Ketterson, L. R. Windmiller, S. Hörnfeldt, and F. M. Mueller, Solid State Commun. **6,** 851 (1968).
[16] J. C. Phillips, Phys. Rev. **140,** A1254 (1965).
[17] J. B. Ketterson and L. R. Windmiller, Phys. Rev. B **1,** 463 (1970).
[18] D. J. Roaf, Phil. Trans. Roy. Soc. London **A255,** 135 (1962).
[19] M. R. Halse, Phil. Trans. Roy. Soc. London **265,** 507 (1969).
[20] J. B. Ketterson, F. M. Mueller, and L. R. Windmiller, Phys. Rev. **186,** 656 (1969).
[21] B. Bosacchi, J. B. Ketterson, and L. R. Windmiller, Phys. Rev. B **2,** 3019 (1970).
[22] L. R. Windmiller and J. B. Ketterson, Phys. Rev. Letters **21,** 1076 (1968).
[23] F. M. Mueller, L. R. Windmiller and J. B. Ketterson, J. Appl. Phys. **41,** 2312 (1970).
[24] O. K. Andersen, Ph.D. thesis, Technical University, Lyngby, Denmark, 1969 (unpublished).
[25] N. E. Alekseevskii and Yu. Gaidukov, Zh. Eksperim. i Teor. Fiz. **38,** 1720 (1960) [Soviet Phys. JETP **11,** 1242 (1960)]; N. E. Alekseevskii, V. V. Mozhaev and G. E. Karstens, in *Pro-*

ceedings of the Tenth International Conference on Low Temperature Physics, Moscow, U.S.S.R., 31 August–6 September 1966 (Vimiti Publishing House, Moscow, 1966).
[26] M. D. Stafleu and A. R. de Vroomen, Phys. Letters **19,** 81 (1965).
[27] J. B. Ketterson, M. G. Priestley, and J. J. Vuillemin, Phys. Letters **20,** 452 (1966).
[28] J. B. Ketterson and L. R. Windmiller, Phys. Rev. Letters **20,** 321 (1968).
[29] L. R. Windmiller and J. B. Ketterson, Phys. Rev. Letters **20,** 324 (1968).
[30] L. R. Windmiller, J. B. Ketterson, and S. Hörnfeldt, J. Appl. Phys. **40,** 1291 (1969).
[31] R. W. Stark and L. R. Windmiller, Cryogenics **8,** 272 (1968).
[32] L. R. Windmiller and J. B. Ketterson, Rev. Sci. Instr. **39,** 1672 (1968).
[33] Varian Associates, Palo Alto, Calif.
[34] Texas Instruments Inc., Houston, Tex.
[35] Hysol Corporation, Olean, N.Y.
[36] Sigmund Cohn Corp., Mt. Vernon, N.Y.
[37] R. W. Johnson, J. Appl. Phys. **34,** 352 (1963).
[38] E. Raub and G. Buss, Z. Elektrochem. **46,** 195 (1940).
[39] S. Hörnfeldt, J. B. Ketterson, and L. R. Windmiller, J. Crystal Growth **5,** 289 (1969).
[40] J. B. Ketterson, J. S. Tait, and L. R. Windmiller, J. Crystal Growth **1,** 323 (1967).
[41] R. P. Huebener, Phys. Rev. **146,** 490 (1966).
[42] The zero for the experimental rotator angle ψ was poorly determined for run *a*. This inaccuracy is corrected by the orientation program which finds the value of θ and φ, corresponding to the assumed zero of ψ rather than the values for the sample axis. This results in the values of θ and φ, for run *a* being significantly different than the values for runs *b* and *c*.
[43] D. Shoenberg, Phil. Trans. Roy. Soc. London **A255,** 85 (1962).
[44] J. H. Condon, Phys. Rev. **145,** 526 (1966).
[45] M. Dixon, F. E. Hoare, T. M. Holden, and D. E. Moody, Proc. Roy. Soc. (London) **A285,** 561 (1965).
[46] N. F. Berk and J. R. Schrieffer, Phys. Rev. Letters **17,** 433 (1966).
[47] S. Doniach and S. Engelsberg, Phys. Rev. Letters **17,** 750 (1966).

PHYSICAL REVIEW B VOLUME 2, NUMBER 12 15 DECEMBER 1970

Electrical Properties of Ta_2H†

T. G. BERLINCOURT*
Science Center, North American Rockwell, Thousand Oaks, California 91360
AND
P. W. BICKEL‡
Atomics International, Division of North American Rockwell, Canoga Park, California 91304

(Received 27 July 1970)

Data have been obtained on the electrical resistivity, Hall effect, and thermoelectric power in Ta_2H from low temperatures to above the hydrogen sublattice order-disorder transformation temperatures. Prominent manifestations of the β_1-β_2 and β_2-α transformations are evident in the data, but no clear evidence was found for a splitting of the upper transition such as that reported in the calorimetric studies of Saba *et al.* Several features of the electrical properties are consistent with the existence of similar conduction-electron dispersions in Ta_2H and Ta metal, but other factors appear to be inconsistent with this possibility. Hysteresis was observed in the electrical resistivity in the vicinity of the order-disorder transformations, and possible origins of this hysteresis are discussed. The Hall-effect data show that the majority charge carriers in Ta_2H are holes.

I. INTRODUCTION

Tantalum hydride of nominal composition Ta_2H has been studied extensively both experimentally[1,2] and theoretically.[3] Interest in this interstitial system centers on the order-disorder transformations which take place in the hydrogen sublattice as the temperature is increased. At temperatures below ~308°K, Ta_2H exists in the β_1 form characterized by a pseudotetragonal Ta sublattice with $a \approx b \approx \sqrt{2}a_0$ and $c \approx a_0$, where a_0 is the lattice parameter of bcc Ta metal. Neutron scattering experiments[4] on Ta_2D have been interpreted[5] as evidence that the hydrogen atoms in $\beta_1 = Ta_2H$ occupy the tetrahedral positions $(\frac{1}{4}\ \frac{1}{4}\ \frac{1}{4})$ and $(\frac{1}{4}\ \frac{3}{4}\ \frac{3}{4})$, so that in this phase long-range order exists in the hydrogen sublattice. This order is partially destroyed in β_2-Ta_2H, which exists between ~308 and ~332°K. Evidence from specific-heat measurements by Saba *et al.*[6] suggests that still another form, β_3-Ta_2H, might exist over a small temperature range (~2°K) above ~332°K, but electrical-resistance data reported by Wallace[4] show no evidence to support this possibility. Finally, above ~334°K the interstitial hydrogen is thought to be completely disordered, and the Ta sublattice assumes the bcc or α structure characteristic of Ta metal.

The work reported here was undertaken with the hope that more extensive data on the electrical properties would shed light on the nature of the order-disorder transformations and on the way in which addition of hydrogen to Ta influences the electronic structure. Some of the results presented below are consistent with a high degree of similarity between the conduction-electron structures in Ta_2H and in pure Ta metal, but other factors are in seeming conflict with this interpretation.

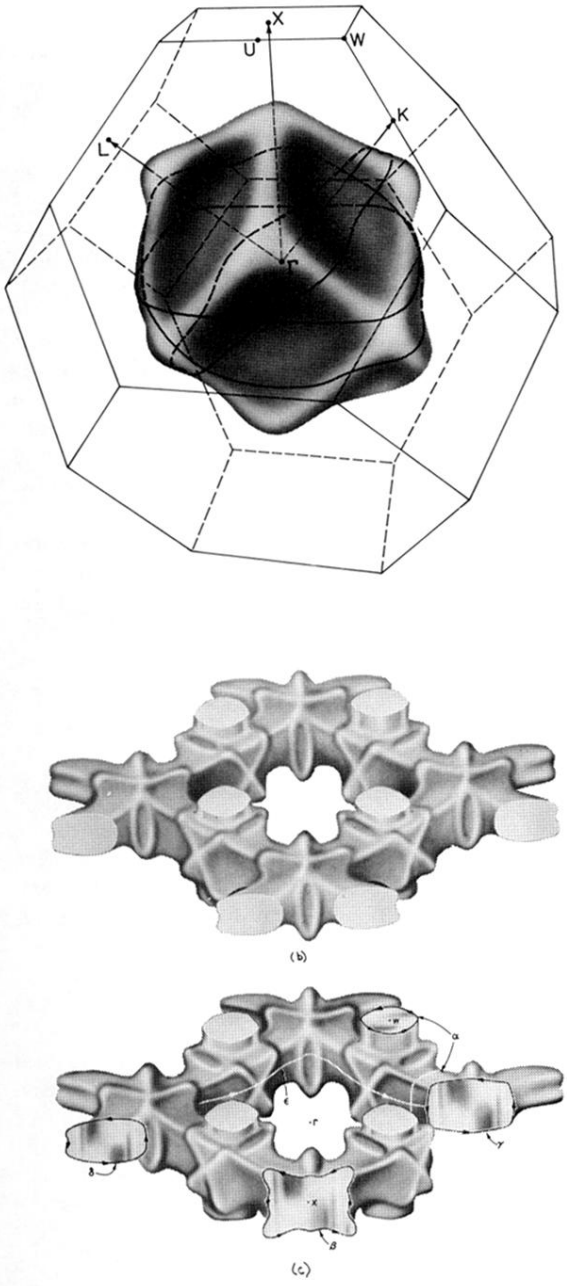

FIG. 5. (a) Electron Fermi surface of Pt. (b) Open sheet of the Fermi surface of Pt showing connectivity, viewed from approximately the ⟨111⟩ direction. (c) Cutaway of the open sheet of the Fermi surface of Pt showing the α, β, γ, and δ orbits (in a magnetic field).